Discovery of novel putative tumor suppressors from CRISPR screens reveals rewired lipid metabolism in AML cells

W. Frank Lenoir[1,2], Micaela Morgado[2], Peter C DeWeirdt[3], Megan McLaughlin[1,2], Audrey L Griffith[3], Annabel K Sangree[3], Marissa N Feeley[3], Nazanin Esmaeili Anvar[1,2], Eiru Kim[2], Lori L Bertolet[2], Medina Colic[1,2], Merve Dede[1,2], John G Doench[3], Traver Hart[2,4,*]

1 - The University of Texas MD Anderson Cancer Center UTHealth Graduate School of Biomedical Sciences; The University of Texas MD Anderson Cancer Center, Houston, TX

2 - Department of Bioinformatics and Computational Biology, The University of Texas MD Anderson Cancer Center, Houston, TX, USA

3 - Genetic Perturbation Platform, Broad Institute of MIT and Harvard, Cambridge, MA, USA

4 - Department of Cancer Biology, The University of Texas MD Anderson Cancer Center, Houston, TX, USA

* - Corresponding author: traver@hart-lab.org

Abstract

CRISPR knockout screens in hundreds of cancer cell lines have revealed a substantial number of context-specific essential genes that, when associated with a biomarker such as lineage or oncogenic mutation, offer candidate tumor-specific vulnerabilities for targeted therapies or novel drug development. Data-driven analysis of knockout fitness screens also yields many other functionally coherent modules that show emergent essentiality or, in rarer cases, the opposite phenotype of faster proliferation. We develop a systematic approach to classify these suppressors of proliferation, which are highly enriched for tumor suppressor genes, and define a network of 145 genes in 22 discrete modules. One surprising module contains several elements of the glycerolipid biosynthesis pathway and operates exclusively in a subset of AML lines, which we call Fatty Acid Synthesis/Tumor Suppressor (FASTS) cells. The proliferation suppressor activity of genes involved in the synthesis of saturated fatty acids, coupled with a more severe fitness phenotype for the desaturation pathway, suggests that these cells operate at the limit of their carrying capacity for saturated fatty acids, which we confirmed biochemically. Overexpression of genes in this module is associated with a survival advantage in an age-matched cohort of AML patients, suggesting the gene cluster driving an *in vitro* phenotype may be associated with a novel, clinically relevant subtype.

Introduction

Gene knockouts are a fundamental tool for geneticists, and the discovery of CRISPR-based genome editing[1] and its adaptation to gene knockout screens has revolutionized mammalian functional genomics and cancer targeting[2–8]. Hundreds of CRISPR/Cas9 knockout screens in cancer cell lines have revealed background-specific genetic vulnerabilities[9–13], providing guidance for tumor-specific therapies and the development of novel targeted agents. Although lineage and mutation state are powerful predictors of context-dependent gene essentiality, variation in cell growth medium and environment can also drive differences in cell state, particularly among metabolic genes[14,15], and targeted screening can reveal the genetic determinants of metabolic pathway buffering[16,17].

The presence and composition of metabolic and other functional modules in the cell can also be inferred by integrative analysis of large numbers of screens. Correlated gene knockout fitness profiles, measured across hundreds of screens, have been used to infer gene function and the modular architecture of the human cell[18–21]. Data-driven analysis of correlation networks reveals clusters of functionally related genes whose emergent essentiality in specific cell backgrounds is often unexplained by the underlying lineage or mutational landscape[21]. Interestingly, in a recent study of paralogs whose functional buffering renders them systematically invisible to monogenic CRISPR knockout screens[22,23], it was shown that the majority of context-dependent essential genes are constitutively expressed in cell lines[23]. Collectively these observations suggest that there is much unexplained variation in the genetic architecture, and emergent vulnerability, of tumor cells.

Building human functional interaction networks from correlated gene knockout fitness profiles in cancer cells is analogous to generating functional interaction networks from correlated genetic interaction profiles in *S. cerevisiae*[24–27]. The fundamental difference between the two approaches is that, in yeast, a massive screening of pairwise gene knockouts in a single yeast strain was conducted in order to measure genetic interaction - a dual knockout phenotype more or less severe than that expected by the combination of the two genes independently. In coessentiality networks, CRISPR-mediated single gene knockouts are conducted across a panel of cell lines that sample the diversity of cancer genotypes and lineages. Digenic perturbations in human cells, a more faithful replication of the yeast approach, are possible with Cas9 and its variants, but

library construction, sequencing, and positional biases can be problematic[16,28–34]. Recently, we showed that an engineered variant of the Cas12a endonuclease, enCas12a[35], could efficiently perform multiplex gene knockouts[34], and we demonstrated its effectiveness in assaying synthetic lethality between targeted paralogs[23]. These developments in principle enable researchers to measure how biological networks vary across backgrounds, a powerful approach for deciphering complex biology[24,36,37].

CRISPR perturbations in human cells can result in loss of function alleles that increase as well as decrease *in vitro* proliferation rates; faster proliferation is an extreme rarity in yeast knockouts. These fast-growers can complicate predictions of genetic interaction[29] and confound pooled chemoresistance screens[38]. However, there is no broadly accepted method of identifying these genes from CRISPR screens. Here we describe the development of a method to systematically classify genes whose knockout provides a proliferation advantage *in vitro*. We observe that genes which confer proliferation advantage are typically tumor suppressor genes, and that they show the same modularity and functional coherence as context-dependent essential genes. Moreover, we discover a novel module that includes several components of the glycerolipid biosynthesis pathway that slows cell proliferation in a subset of acute myeloid leukemia (AML) cell lines. We show a rewired genetic interaction network using enCas12a multiplex screening, and find strong genetic interactions corroborated by clinical survival data. A putative tumor-suppressive role for glycerolipid biosynthesis is surprising and disconcerting, since this process is thought to be required to generate biomass for tumor cell growth, and inhibitors targeting this pathway are currently in clinical trials[39,40].

Results

Identifying Proliferation Suppressor Signatures

We previously observed genes whose knockout leads to overrepresentation in pooled library knockout screens. These genes, which we term proliferation suppressor genes (PSG), exhibit positive selection in fitness screens, a phenotype opposite that of essential genes. As expected, many PSG are known tumor suppressor genes; for example, *TP53* and related pathway genes *CDKN1A*, *CHEK2*, and *TP53BP1* show positive selection in select cell lines (**Figure 1a**). Detection of these genes as outliers is robust to the choice of CRISPR analytical method, as we tested BAGEL2[41,42], CERES[10], JACKS[43], and mean log fold change (LFC) of gRNA targeting each

114 gene (**Supplementary Figure 1a-d**). Unlike core-essential genes, PSG are highly context-
115 specific: *TP53* knockout shows positive LFC only in cell lines with wild-type *TP53* (**Figure 1b**),
116 and *PTEN* knockout shows the PS phenotype only in $PTEN^{wt}$ backgrounds (**Figure 1c**). These
117 observations are consistent with the knockout phenotypes of known tumor suppressor genes
118 (TSG) in cell lines: in wildtype cells, TSG knockout increases the proliferation rate in cell culture,
119 but when cell lines are derived from tumors where the TSG is already lost or non-functional, gene
120 knockout has no effect. TSG are therefore context-specific PSG, but it is not necessarily the case
121 that genes with a proliferation suppressor phenotype *in vitro* act as TSG *in vivo;* proliferation
122 suppressors are at best putative tumor suppressors in the absence of confirmatory data from
123 tumor profiling.
124
125 Though detection of PSG is possible using existing informatics pipelines, several factors
126 complicate a robust detection of these genes. There is no accepted threshold for any algorithm
127 we considered to detect PSG, since all were optimized to classify essential genes. A related
128 second issue is that cell line screens show a wide range of variance in LFC distributions, making
129 robust outlier detection challenging (**Supplementary Figure 1e-f**). Third, the signatures are
130 strongly background-dependent, as demonstrated by PTEN and TP53. Finally, there is no
131 consistent expectation for whether or how many putative tumor suppressor genes are present in
132 a given cell line.
133
134 To address this gap, we developed a method to account for variability in fold-change distributions
135 between screens. Our approach uses a Gaussian mixture model (K=2) to estimate each screen's
136 distribution of gene-level LFC scores (**Figure 1a**). Mixed distribution models have previously been
137 used to identify distinctions between populations of essential and nonessential fitness genes in
138 CRISPR screens[44]. For the K = 2 mixture model, the more negative distribution (**Figure 1a**, red)
139 is generally essential genes, while the higher, narrower peak around zero (**Figure 1a**, blue),
140 models the large population of knockouts with no fitness phenotype. We used this second model
141 to calculate a Z-score (hereafter referred to as the 'mixed Z-score') for all gene-level mean fold
142 changes in each cell line. This approach normalizes variance (**Supplementary Figure 1e-f**)
143 across LFC distributions in different cell lines, with negative Z-scores indicating essential genes
144 and positive Z-scores representing PSG phenotypes.
145
146 To evaluate the effectiveness of this mixed Z-score approach, we used COSMIC[45,46] tumor
147 suppressor genes as a true positive reference set, and we combined COSMIC-defined oncogenes

148 (removing dual-annotated tumor suppressors) with our previously-specified set of nonessential
149 genes as a true negative reference set[7,47]. Since there is no expectation for the presence of a
150 consistent set of PSG across cell lines, we analyzed each of the 808 cell lines from the Avana
151 2020Q4 data release independently[10,48,49] calculating gene-level scores on each cell line
152 individually and then combining all scores into a master list of 808 x 18k = 14.6 million gene-cell
153 line observations (**Supplementary Table 1**). Moreover, since there is also no expectation that all
154 COSMIC TSG would be detected cumulatively across all cell lines, we judged that traditional recall
155 metrics (e.g. percentage of the reference set recovered) were inappropriate. We therefore defined
156 recall as the total number of TSG-cell line observations. Using this evaluation scheme, the mixed
157 Z-score approach outperforms comparable methods by a substantial margin, classifying more
158 than 722 PS-cell line instances at a 10% false discovery rate (FDR) (**Figure 1d**). This is roughly
159 50% more putative PSG than the closest alternative, a nonparametric rank-based approach, at
160 the same FDR. BAGEL[41,42], a supervised classifier of essential genes, performed worst at TSG,
161 and the raw mean LFC approach also fared poorly, highlighting the need for variance
162 normalization across experiments. We applied this 10% FDR threshold for all subsequent
163 analyses.
164
165 Common tumor suppressor genes PTEN and TP53 were observed in ~15% of cell lines (**Figure**
166 **1e**), with other well-known TSG appearing less frequently. Among 309 COSMIC TSGs for which
167 we have fitness profiles (representing 1.7% of all 18k genes), we find that 116 (37.5%) of these
168 genes occur as proliferation suppressors at least once (**Supplementary Table 2**) and make up
169 24.4% of total proliferation suppressor calls (**Supplementary Figure 2a-b**), a 14-fold enrichment.
170 All of the known TSG hits come from just 504 of the 808 cell lines (62.4%) in which proliferation
171 suppressor hit calls were identified (**Figure 1f**), yet we did not observe a bias toward particular
172 tissues: in every lineage, most cell lines carried at least one PSG (**Supplementary Figure 1g**).
173
174 To further validate our approach, we compared the set of TSGs in our PSG hits to other molecular
175 profiling data. When identified as a proliferation suppressor, 53% of the 116 TSGs demonstrate
176 higher mean mRNA expression relative to backgrounds where the same TSG is not a proliferation
177 suppressor (**Supplementary Table 2**). Similarly, 96.6% of the 116 TSGs, when classified as a
178 proliferation suppressor, demonstrate lower frequency of nonsilent mutations compared to
179 backgrounds where the TSG is not a hit (**Supplementary Table 2**). These observations were not
180 restricted to COSMIC TSGs however, as this was the case for all PSG hit calls of genes against
181 non-PSG hit calls (**Supplementary Figure 2c** and **2d**). Copy number comparisons did not

182 suggest major distinctions between PSG vs non-PSG calls (**Supplementary Figure 2e)**, however
183 there did appear to be more variation in PSG observations, possible stemming from smaller
184 grouped sample sizes. Together, these observations confirm the reliability of our method to detect
185 genes whose knockout results in faster cell proliferation, and that, analogous to essential genes,
186 these genes must be expressed and must not harbor a loss-of-function mutation in order to elicit
187 this phenotype.
188
189 We attempted to corroborate our findings using a second CRISPR dataset of 342 cell line screens
190 from Behan *et al.*[13], including >150 screens in the same cell lines as in the Avana data. However,
191 these screens were conducted over a shorter timeframe than the Avana screens (14 vs. 21 days),
192 giving less time for both positive and negative selection signals to appear (see Methods for a
193 detailed discussion). As a result, when we compared cell lines screened by both groups, the
194 Avana data yielded many more TSG hits (**Supplementary Figure 3a**). While most of these do
195 not meet our threshold for PSG in the Sanger data, hits at our 10% FDR threshold across all
196 Avana screens are strongly biased toward positive mixed Z-scores in the Sanger screens
197 (**Supplementary Figure 3b**), consistent with a weaker signal of positive selection as a result of
198 the shorter assays rather than a lack of robustness in the screens[49].
199
200 ***Discovering Pathways Modulating Cell Growth with a Proliferation Suppressor Co-***
201 ***Occurrence Network***
202
203 Although known TSG act as PSG in only a subset of cell lines, we observed patterns of co-
204 occurrence among functionally related genes. *PTEN* co-occurs with mTOR regulators *NF2*[50] ($P <$
205 $3x10^{-11}$, Fisher's exact test) and the *TSC1*/*TSC2* complex (P-values both $< 7x10^{-13}$)[51], as well as
206 Programmed Cell Death 10 (*PDCD10*)[52], a proposed tumor suppressor[7,53] (**Figure 2a**). The p53
207 regulatory cluster (*TP53*, *CDKN1A*, *CHECK2*, *TP53BP1*) also exhibited a strong co-occurrence
208 pattern that was independent of the mTOR regulatory cluster (**Figure 2a**). mTOR[54] and cell cycle
209 checkpoint genes[55,56] have been heavily linked to cancer development, given their roles in
210 controlling cell growth and proliferation, and thus have been the focus of studies characterizing
211 patient genomic profiles to identify common pathway alterations[57,58].
212
213 The modularity of mTOR regulators and TP53 regulators demonstrates pathway-level
214 proliferation suppressor activity. This reflects the concept of genes with correlated fitness profiles
215 indicating the genes operate in the same biochemical pathway or biological process[19,21,59,60].

216 However, the sparseness of PSG, coupled with their smaller effect sizes, renders correlation
217 networks relatively poor at identifying modules of genes with proliferation suppressor activity. In
218 order to identify such modules, we developed a PSG network (**Supplementary Table 3)** based
219 on statistical overrepresentation of co-occurring PSG (**Figure 2b**); see Methods for details. This
220 approach yields a network of 145 genes containing 462 edges in disconnected clusters; only 8
221 clusters have 3 or more genes (**Figure 2c** and **Supplementary Figure 4c**). Of these 462 edges,
222 74 (16.0%, empirical $P<10^{-4}$) are present in the HumanNet[61] functional interaction network
223 (**Supplementary Figure 4a-b**),~8 fold more than expected from random sampling, indicating high
224 functional coherence between connected genes. The network recovers the PTEN and TP53
225 modules as well as the Hippo pathway, the aryl hydrocarbon receptor complex (AHR/ARNT), the
226 mTOR-repressing GATOR1 complex, the STAGA chromatin remodeling complex, JAK-STAT
227 signaling, and the gamma-secretase complex (**Figure 2c, and Supplementary 4c**), all of which
228 have been associated with tumor suppressor activity. The functional coherence and biological
229 relevance of the PSG co-occurrence network further validates the approach taken and establishes
230 this dataset as a resource for exploring putative tumor suppressor activity in cell lines and tumors.
231
232 ***Variation in Fatty Acid Metabolism in AML Cells***
233
234 In addition to the known tumor suppressors, we observed a large module containing elements of
235 several fatty acid (FA) and lipid biosynthesis pathways (**Figure 2c**). Interestingly, while there does
236 not appear to be a strong tissue specificity signature for most clusters (**Figure 2c**), the fatty acid
237 metabolism cluster shows a strong enrichment for AML cell lines ($P = 1.5x10^{-4}$). AML, like most
238 cancers, typically relies on increased glucose consumption for energy and diversion of glycolytic
239 intermediates for the generation of biomass required for cell proliferation. Membrane biomass is
240 generated by phospholipid biosynthesis that uses fatty acids as building blocks, with FA pools
241 replenished by some combination of triglyceride catabolism, transporter-mediated uptake, and *de*
242 *novo* synthesis via the *ACLY/ACACA/FASN* palmitate production pathway using citrate precursor
243 diverted from the TCA cycle. Indeed, the role of lipid metabolism in AML progression is indicated
244 by changes in serum lipid content[62], in particular for long-chain saturated fatty acids that are the
245 terminal product of the FAS pipeline. Inhibition of FA synthesis is therefore an appealing
246 chemotherapeutic intervention[63,64] and FASN inhibitors are currently undergoing clinical trials for
247 treatment of solid tumors and metabolic diseases[40]. The observation that knocking out FAS
248 pathway genes results in *faster* proliferation in some AML cells, and their signature as putative
249 tumor suppressor genes, is therefore very unexpected.

250

251 To learn whether additional elements of lipid metabolism were associated with the FAS cluster,
252 we examined the differential correlation of mixed Z-scores in AML cells. We and others have
253 shown that genes with correlated gene knockout fitness profiles in CRISPR screens are likely to
254 be involved in the same biological pathway or process ("co-functional")[18–21], analogous to
255 correlated genetic interaction profiles in yeast[25,26,65]. Strikingly, all gene pairs within the fully
256 connected clique in the FAS cluster (containing genes *FASN*, *ACACA*, *GPAT4*, *CHP1*, *GPI*
257 *CERS6, PCGF1,* **Figure 2c**) had a median Pearson correlation coefficient (PCC) of 0.76 in the
258 23 AML cell lines (range 0.63-0.95, **Figure 3a**, red), compared to median correlation of 0.05 in
259 the remaining 785 cell lines (range -0.11-0.62, with the highest correlation between *FASN* and
260 *ACACA*, adjacent enzymes in the linear palmitate synthesis pathway; **Figure 3a,** gray). These
261 high differential Pearson correlation coefficients (dPCC) suggest that variation in lipid metabolism
262 is pronounced in AML cells[66].
263

264 We sought to explore whether this difference in correlation identified other genes that might give
265 insight into metabolic rewiring in AML. We first removed noisy data by filtering for high-quality
266 screens (Cohen's D > 2.5, recall > 60%[42]), leaving 659 cell lines, including 17 AML cell lines.
267 Calculating a global difference between PCC of all gene pairs in all 17 AML and in the remaining
268 642 cell lines yielded many gene pairs whose dPCC appeared indistinguishable from random
269 sampling (**Supplementary Figure 5a-b**). To filter these, we calculated empirical P-values for
270 each gene pair. We randomly selected 17 cell lines from the pool of all screens, calculated PCC
271 for all gene pairs in the selected and remaining lines, and calculated dPCC from these PCC values
272 (**Figure 3b**). We repeated this process 1,000 times to generate a null distribution of dPCC values
273 for each gene pair, against which a P-value could be computed (**Figure 3c-d**).
274

275 Expanding the set to a filtered list of genes whose correlation with a gene in the FAS clique
276 showed significant change in AML cells (P<0.001; see Methods) yielded a total of 106 genes,
277 including the 7 genes in the clique (**Figure 3e**) plus Holocarboxylase Synthetase (*HLCS*), which
278 biotinylates and activates acetyl-CoA-carboxylase, the protein product of *ACACA*, as well as
279 glycolysis pathway genes *PGP* and *HK2*. Interestingly, about half of the genes showed
280 significantly increased anticorrelation with the FAS cluster, indicating genes preferentially
281 essential where the FAS genes act as proliferation suppressors (**Figure 3e**). These genes include
282 fatty acid desaturase (*SCD*), which operates directly downstream from *FASN/ACACA* to generate

283 monounsaturated fatty acid species, and Sterol Regulatory Element Binding Transcription Factor
284 1 (*SREBF1*), the master regulatory factor for lipid homeostasis in cells.
285
286 Clustering the AML cells lines according to these high-dPCC genes reveals two distinct subsets
287 of cells. The FAS cluster and its correlates show strong proliferation suppressor phenotype in four
288 cell lines, NB4, MV411, MOLM13, and THP1. The remaining thirteen AML cell lines show
289 negligible to weakly essential phenotypes when these genes are knocked out. The anticorrelated
290 genes, including *SCD* and *SREBF1*, show heightened essentiality in these same cell lines.
291 Together these observed shifts in gene knockout fitness indicates that this subset of AML cells
292 has a substantial metabolic rewiring. Because these cells share a genetic signature among fatty
293 acid synthesis pathway genes that is consistent with tumor suppressors, we call these cell lines
294 Fatty Acid Synthesis/Tumor Suppressor (FASTS) cells (**Figure 3e**).
295
296 ***Cas12a-mediated Genetic Interaction Screens Confirm Rewired Lipid Metabolism***
297
298 We sought to confirm whether gene knockout confers improved cell fitness, and to gather some
299 insight into why some AML cells show the FASTS phenotype and others do not. Genetic
300 interactions have provided a powerful platform for understanding cellular rewiring in model
301 organisms, and we sought to apply this approach to deciphering the FASTS phenotype. We
302 designed a CRISPR screen that measures the genetic interactions between eight selected "query
303 genes" and ~100 other genes ("array genes"). The query genes include *FASN* and *ACACA*, from
304 the cluster of proliferation-suppressor genes, as well as lipid homeostasis transcription factor
305 *SREBF1*, anticorrelated with the FAS cluster in the differential network analysis, and
306 uncharacterized gene *c12orf49*, previously implicated in lipid metabolism by coessentiality[21] and
307 a recent genetic interaction study[60]. Additional query genes include control tumor suppressor
308 genes *TP53* and *PTEN* and control context-dependent essential genes *GPX4* and *PSTK (***Figure**
309 **4a***).* The array genes include two to three genes each from several metabolic pathways, including
310 various branches of lipid biosynthesis, glycolysis and glutaminolysis, oxphos, peroxisomal and
311 mitochondrial fatty acid oxidation. We include the query genes in the array gene set (**Figure 4a**)
312 to test for screen artifacts and further add control essential and nonessential genes to measure
313 overall screen efficacy (**Supplementary Table 4-5**).
314
315 We used the enCas12a CRISPR endonuclease system to carry out multiplex gene knockouts[35].
316 We used a dual-guide enCas12a design, as described in DeWeirdt *et al.*[34], that allows for

317 construction of specific guide pairs through pooled oligonucleotide synthesis (**Figure 4b**). The
318 library robustly measures single knockout fitness by pairing three Cas12a crRNA per target gene
319 each with five crRNA targeting nonessential genes[7,47] (n=15 constructs for single knockout
320 fitness), and efficiently assays double knockout fitness by measuring all guides targeting query-
321 array gene pairs (n=9) (**Figure 4c & Supplementary Table 5**). Using this efficient design and the
322 endogenous multiplexing capability of enCas12a, we were able to synthesize a library targeting
323 800 gene pairs with a single 12k oligonucleotide array.
324
325 We screened one AML cell line from the FASTS subset, MOLM13, and a second one with no FAS
326 phenotype, NOMO1, collecting samples at 14 and 21 days after transduction with a five-day
327 puromycin selection (**Supplementary Table 6-7**). Importantly, by comparing the mean log fold
328 change of query gene knockouts in the "A" position *vs.* the same genes in the "B" position of the
329 dual knockout vector, we find no positional bias in the multiplex knockout constructs (**Figure 4d**),
330 consistent with our previous findings[23,34]. Single knockout fitness measurements effectively
331 segregated known essential genes from nonessentials, confirming the efficacy of the primary
332 screens (**Supplementary Figure 6**). Context-dependent fitness profiles are consistent with the
333 cell genotypes, with *PTEN* and *TSC1* showing positive selection in *PTEN*^{wt} NOMO1 cells and
334 *TP53* being a strong PS gene in *P53*^{wt} MOLM13 cells. Strikingly, *CHP1* and *GPAT4* are the next
335 two top hits in MOLM13, confirming their proliferation suppressor phenotype (**Figure 4e**), while
336 neither shows a phenotype in NOMO1. Together these observations validate the enCas12a-
337 mediated multiplex perturbation platform, confirm the ability of CRISPR knockout screens to
338 detect proliferation suppressors, and corroborate the background-specific fitness enhancing
339 effects of genes from the FAS cluster.
340
341 To measure genetic interactions, we fit a linear regression for each guide between the
342 combination LFCs and the single guide LFCs, Z-scoring the residuals from this line, and
343 combining across all guides targeting the same gene pair (**Supplementary Figure 6 &**
344 **Supplementary Table 7**). Here, positive genetic interaction Z-scores reflect greater fitness than
345 expected and negative Z-scores represent lower than expected based on the single gene
346 knockouts independently, similar to the methodology applied in a recent survey of genetic
347 interactions in cancer cells using multiplex CRISPR perturbation[33] (see Methods). Gene self-
348 interactions (when the same gene is in the A and B position, **Figure 4d**) should therefore be
349 negative for proliferation suppressors and positive for essentials (**Figure 4f-g**, **Supplementary**
350 **Figure 6**). Overall, genetic interaction Z-scores in the two cell lines showed moderate correlation

351 (**Figure 4g**) and previously reported synthetic interactions between *C12orf49* and low-density
352 lipoprotein receptor *LDLR*[17] and between *SREBF1* and its paralog *SREBF2*[17] are identified in both
353 cell lines (**Supplementary Figure 6f-g**).
354
355 In contrast with the interactions found in both cell lines, background-specific genetic interactions
356 reflect the genotypic and phenotypic differences between the cells. The negative interaction
357 between tumor suppressor *PTEN* and mTOR repressor *TSC1* in *PTEN*^{wt} NOMO1 cells is
358 consistent with their epistatic roles in the mTOR regulatory pathway. Both genes show positive
359 knockout fitness in NOMO1 (**Figure 4e**) but their dual knockout does not provide an additive
360 growth effect, resulting in a suppressor interaction with a negative Z-score (**Figure 4g-h**).
361 Similarly, suppressor genetic interactions between *ACACA* and downstream proliferation
362 suppressor genes *CHP1* and *GPAT4* are pronounced in MOLM13 cells, consistent with epistatic
363 relationships in a linear biochemical pathway (**Figure 4h**). These interactions are not replicated
364 with query gene *FASN*, but both *FASN* and *ACACA* show negative interactions with fatty acid
365 transport gene *FABP5* and positive interactions with *SREBF1* and *SCD,* the primary desaturase
366 of long-chain saturated fatty acids. All of these interactions are absent in NOMO1, demonstrating
367 the rewiring of the lipid biosynthesis genetic interaction network between these two cell types
368 (**Figure 4h**).
369
370 ***FASTS Signature Predicts Sensitivity to Saturated Fatty Acids***
371
372 The significant differences in the single- and double-knockout fitness signatures between the two
373 cell lines suggests a major rewiring of lipid metabolism in these cells. *CHP1* and *GPAT4* are
374 reciprocal top correlates in the Avana coessentiality network ($r = 0.43$, $P = 2.5\times10^{-34}$), strongly
375 predicting gene co-functionality[21]. Two recent studies characterized the role of lysophosphatidic
376 acid acyltransferase *GPAT4* in adding saturated acyl moieties to glycerol 3-phosphate, generating
377 lysophosphatidic acid (LPA) and phosphatidic acid (PA), the precursors for cellular phospholipids
378 and triglycerides, and further discovered *CHP1* as a key regulatory factor for *GPAT4* activity[67,68].
379 Within hematological cancer cell lines, the coessentiality network is significantly restructured, with
380 the *ACACA*/*FASN* module correlated with *SCD* in most backgrounds ($r = 0.35$, $P < 10^{-18}$) but
381 strongly anticorrelated in 36 blood cancer cell lines ($r = -0.52$, $P < 10^{-3}$, **Figure 3e**). The magnitude
382 of this change in correlation is ranked #8 out of 31 million gene pairs (see Methods). In contrast,
383 *ACACA* and *FASN* are weakly correlated with *CHP1* in most tissues but strongly correlated in
384 AML, with underlying covariation largely driven by the PS phenotype in FASTS cells (**Figure 3e**).

385 This pathway sign reversal is confirmed in the single knockout fitness observed in our screens:
386 *SCD* is strongly essential in MOLM13 but not in NOMO1 (**Figure 4e**).
387
388 Collectively these observations make a strong prediction about the metabolic processing of
389 specific lipid species. Faster proliferation upon knockout of genes related to saturated fatty acid
390 processing, coupled with increased dependency on fatty acid desaturase gene *SCD* (**Figure 5a**),
391 suggests that these cells are at or near their carrying capacity for saturated fatty acids. To test
392 this prediction, we exposed three FASTS cell lines and four other AML cell lines to various species
393 of saturated and unsaturated fatty acids. FASTS cells showed significantly increased apoptosis
394 in the presence of 200 μm palmitate (**Figure 5b-c**) while no other species of saturated or
395 unsaturated fatty acid showed similar differential sensitivity. In addition, analysis of metabolic
396 profiles of cells in the Cancer Cell Line Encyclopedia[69,70] showed that saturated acyl chains are
397 markedly overrepresented in triacylglycerol (TAG) in FASTS cells (**Figure 5d**), in contrast with
398 other lipid species measured **(Supplementary Figure 7**). Palmitate-induced lipotoxicity has been
399 studied in many contexts – and importantly, the role of *GPAT4* and *CHP1* in mediating lipotoxicity
400 was well described recently[67,68] – but, to our knowledge, this is the first instance of a genetic
401 signature that predicts liposensitivity.
402
403 ***Prognostic signature for FASTS genes***
404
405 To explore whether the FASTS phenotype has clinical relevance, we compared our results with
406 patient survival information from public databases. Using genetic characterization data from
407 CCLE[69], we did not find any lesion which segregated FASTS cells from other CD33+ AML cells
408 (**Figure 6a**), so no mutation is nominated to drive a FASTS phenotype *in vivo*. Instead, we
409 explored whether variation in gene expression was associated with patient outcomes. We
410 included genes in the core FASTS module as well as genes with strong genetic interactions with
411 *ACACA/FASN* in our screen (**Figure 6a**). To select an appropriate cohort for genomic analysis,
412 we first considered patient age. Although AML presents across every decade of life, patients from
413 whom FASTS cell lines were derived are all under 30 years of age (sources of other AML cells
414 ranged from 6 to 68 years; **Figure 6b**). With this in mind, we explored data from the TARGET-
415 AML[71] project, which focuses on childhood cancers (**Figure 6c**). Using TARGET data, we
416 calculated hazard ratios using univariate Cox proportional-hazards modeling with continuous
417 mRNA expression values for our genes of interest as independent variables. We observed that
418 4/7 FAS genes, *GPAT4, CHP1, PCGF1*, and *GPI*, show significant, negative hazard ratios (HR),

419 consistent with a tumor suppressor signature (**Figure 6d**), and that no other gene from our set
420 shows a negative HR. Indeed, when stratifying patients from the TARGET cohort with high
421 expression of *GPAT4, CHP1, PCGF1*, and *GPI* (**Figure 6e**), we observe significantly improved
422 survival (P-value = 0.001, **Figure 6f**). These findings are not replicated for *GPAT4, CHP1*, and
423 *GPI* in the TCGA[72] or OHSU[73] tumor genomics data sets, possibly because they sample older
424 cohorts (Polycomb group subunit *PCGF1* is observed to have a HR < 1 within the OHSU cohort,
425 **Supplementary Figure 8a**). However, age is not generally associated with expression of genes
426 in the FAS cluster in either cell lines or tumor samples (**Supplementary Figure 8**).
427
428 **Discussion**
429
430 CRISPR screens have had a profound impact on cancer functional genomics. While research has
431 been mainly focused on essential gene phenotypes, there is still much clinically relevant biology
432 that can be uncovered by examining other phenotypes from a genetic screen. We establish a
433 methodology that can reliably identify the proliferation suppressor phenotype from whole-genome
434 CRISPR knockout genetic screens. This represents, to our knowledge, the first systematic study
435 of this phenotype in the more than 1,000 published screens[8,10,11,13,48].
436
437 The activity of proliferation suppressor genes is inherently context-dependent, rendering global
438 classification difficult. As with context-dependent essential genes, the strongest signal is attained
439 when comparing knockout phenotype with underlying mutation state. For example, wildtype and
440 mutant alleles of classic tumor suppressor examples *TP53* and *PTEN* are present in large
441 numbers of cell lines, enabling relatively easy discrimination of PS behavior in wildtype
442 backgrounds, but most mutations are much more rare, reducing statistical power. Our model-
443 based approach enables the discovery of PS phenotype as an outlier from null-phenotype
444 knockouts. Using this approach, we recover COSMIC-annotated TSGs exhibiting the PS
445 phenotype when wildtype alleles are expressed at nominal levels.
446
447 Co-occurrence of proliferation suppressors follows the principles of modular biology, with genes
448 in the same pathway acting as proliferation suppressors in the same cell lines. We observe
449 background-specific putative tumor suppressor activity for the PTEN pathway, P53 regulation,
450 mTOR signaling, chromatin remodeling, and others. The co-occurrence network also reveals a
451 novel module associated with glycerolipid biosynthesis, which exhibits the PS phenotype in a
452 subset of AML cells. Analysis of the rewiring of the lipid metabolism coessentiality network in AML

453 cells corroborated this discovery, and led us to define the Fatty Acid Synthesis/Tumor Suppressor
454 (FASTS) phenotype in four AML cell lines. A survey of genetic interactions, using the enCas12a
455 multiplex knockout platform, showed major network rewiring between FASTS and other AML cells
456 and revealed strong genetic interactions in FASTS cells with *GPAT4*, a key enzyme in the
457 processing of saturated fatty acids, and its regulator *CHP1*. Collectively these observations
458 suggest that FASTS cells are near some critical threshold for saturated fatty acid carrying
459 capacity, which we validated biochemically by treatment with fatty acids and bioinformatically
460 through analysis of CCLE metabolomic profiles.
461
462 Confirming the clinical relevance of an *in vitro* phenotype can be difficult. No obvious mutation
463 segregates FASTS cells from other AML cells, and with only four cell lines showing the FASTS
464 phenotype, we lack the statistical power to discover associations in an unbiased way. However,
465 by narrowing our search to strong hits from the differential network analyses, we found a
466 significant survival advantage in a roughly age-matched cohort for *GPAT4* and *CHP1*
467 overexpression. This finding points to a wholly novel tumor suppressor signature for our PSG
468 module, though significant further study is necessary to determine whether this gene expression
469 signature confers a similar *in vivo* metabolic rewiring and sensitivity to saturated lipids.
470
471 The combination of genetic, biochemical, and clinical support for the discovery of a novel tumor
472 suppressor module has several implications. First, it provides a clinical signature that warrants
473 further research as a prognostic marker as well as a potential therapeutic target. Second, it
474 demonstrates the power of differential network analysis, and in particular differential genetic
475 interaction networks, to dissect the rewiring of molecular pathways from modular phenotypes.
476 And finally, it suggests that there still may be much to learn from data-driven analyses of large-
477 scale screen data, beyond the low-hanging fruit of lesion/vulnerability associations.
478
479
480

Acknowledgments

This research was performed in partial fulfillment of the requirements for the PhD degree from The University of Texas MD Anderson Cancer Center UTHealth Graduate School of Biomedical Sciences; The University of Texas MD Anderson Cancer Center, Houston, Texas 77030. WFL, MMc, MMo, and TH were supported by NIGMS grant R35GM130119. MC is supported by a Kopchick fellowship and Pauline Altman-Goldstein Foundation Discovery Fellowship. EK is supported by a grant from the Prostate Cancer Foundation. MD is supported by a Schissler Foundation fellowship. TH is a CPRIT Scholar in Cancer Research (RR160032), and is additionally supported by MD Anderson Cancer Center Support Grant P30 CA016672. WFL is supported by the American Legion Auxiliary Fellowship in Cancer Research. This work was supported by the Andrew Sabin Family Foundation Fellowship (TH). Flow cytometry was performed at MDACC's Advanced Cytometry & Sorting Facility supported by the NCI Cancer Center Support Grant P30CA16672.

Author Contributions

WFL performed all PS discovery analysis. MF, AG, AS performed genetic interaction screens and PD, MC performed bioinformatic analysis. WFL, MC, EK, and MD performed all other bioinformatic analysis. MMo and MMc performed lipid profiling experiments. JGD and TH supervised the research. WFL and TH drafted the manuscript and all authors edited it.

Competing Interests

JGD consults for Agios, Maze Therapeutics, Microsoft Research, and Pfizer; JGD consults for and has equity in Tango Therapeutics. WFL is a former consultant for BioAge Labs, and has equity in Kronos Bio Inc.

511 **Figure Legends**

512

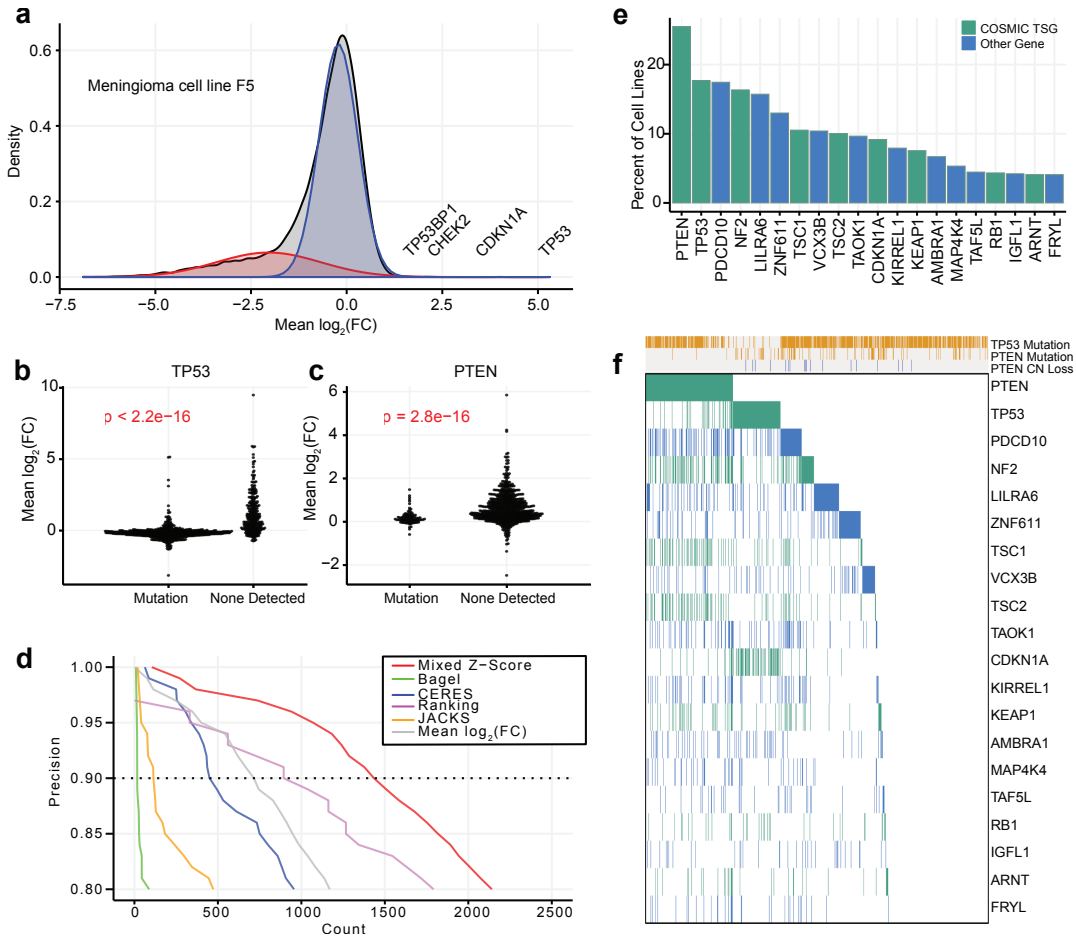

513

514

515 **Figure 1. Discovery of Proliferation Suppressor genes**. (a) Fold-change distribution of a
516 typical CRISPR knockout screen has a long left tail of essential genes, and a small number of
517 genes whose knockout increases fitness (proliferation suppressor genes, “PSG”). A two-
518 component Gaussian mixture model (red, blue) models this distribution. (b) and (c) Fold change
519 of common tumor suppressors across 808 cell lines (P-values, Wilcoxon rank-sum tests). (d)
520 Precision vs. recall of mixed Z-score and other CRISPR analysis methods. Dashed line, 90%
521 precision (10% FDR). (e) Fraction of cell lines in which known tumor suppressors (green) or other
522 genes (blue, not defined as TSG by COSMIC) are classified as PS genes at 10% FDR. (f)
523 Presence of each known TSG across 808 cell lines, vs. cell genetic background. Gold, mutation
524 present; gray, absent. Green or blue, following color scheme in (e), gene is classified as a
525 proliferation suppressor.

526

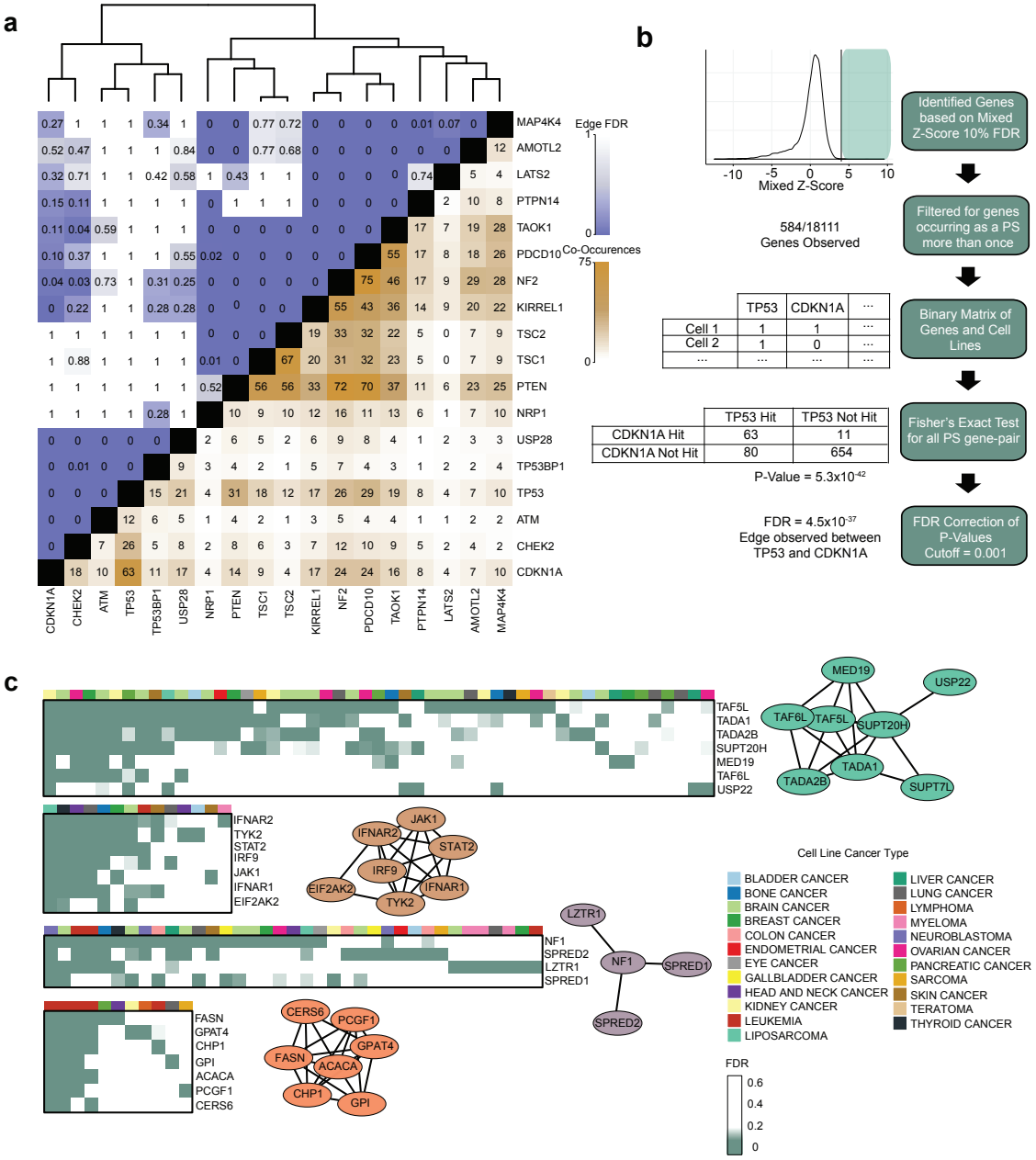
a
b
c
Edge FDR
Co-Occurences
MAP4K4
AMOTL2
LATS2
PTPN14
TAOK1
PDCD10
NF2
KIRREL1
TSC2
TSC1
PTEN
NRP1
USP28
TP53BP1
TP53
ATM
CHEK2
CDKN1A
Mixed Z-Score
584/18111
Genes Observed
Identified Genes based on Mixed Z-Score 10% FDR
Filtered for genes occurring as a PS more than once
Binary Matrix of Genes and Cell Lines
Fisher's Exact Test for all PS gene-pair
FDR Correction of P-Values Cutoff = 0.001
TP53 Hit
TP53 Not Hit
CDKN1A Hit
CDKN1A Not Hit
P-Value = 5.3x10-42
FDR = 4.5x10-37
Edge observed between TP53 and CDKN1A
TAF5L
TADA1
TADA2B
SUPT20H
MED19
TAF6L
USP22
SUPT7L
IFNAR2
TYK2
STAT2
IRF9
JAK1
IFNAR1
EIF2AK2
NF1
SPRED2
LZTR1
SPRED1
FASN
GPAT4
CHP1
GPI
ACACA
PCGF1
CERS6
Cell Line Cancer Type
BLADDER CANCER
BONE CANCER
BRAIN CANCER
BREAST CANCER
COLON CANCER
ENDOMETRIAL CANCER
EYE CANCER
GALLBLADDER CANCER
HEAD AND NECK CANCER
KIDNEY CANCER
LEUKEMIA
LIPOSARCOMA
LIVER CANCER
LUNG CANCER
LYMPHOMA
MYELOMA
NEUROBLASTOMA
OVARIAN CANCER
PANCREATIC CANCER
SARCOMA
SKIN CANCER
TERATOMA
THYROID CANCER
FDR

527

528

529

530 **Figure 2. Co-occurrence of PSG**. (a) Co-occurrence/mutual exclusivity of common TSG as PSG
531 in CRISPR screens. Brown, number of cell lines in which two genes co-occur as PSG at 10%
532 FDR. Blue, FDR of co-occurrence. Hierarchical clustering delineates functional modules. (b)
533 Pipeline for building the co-PS network. (c) Examples from the Co-PS network. Nodes are
534 connected by edges at FDR < 0.1%. Heatmaps indicate presence of PSG vs. cell lineage.
535

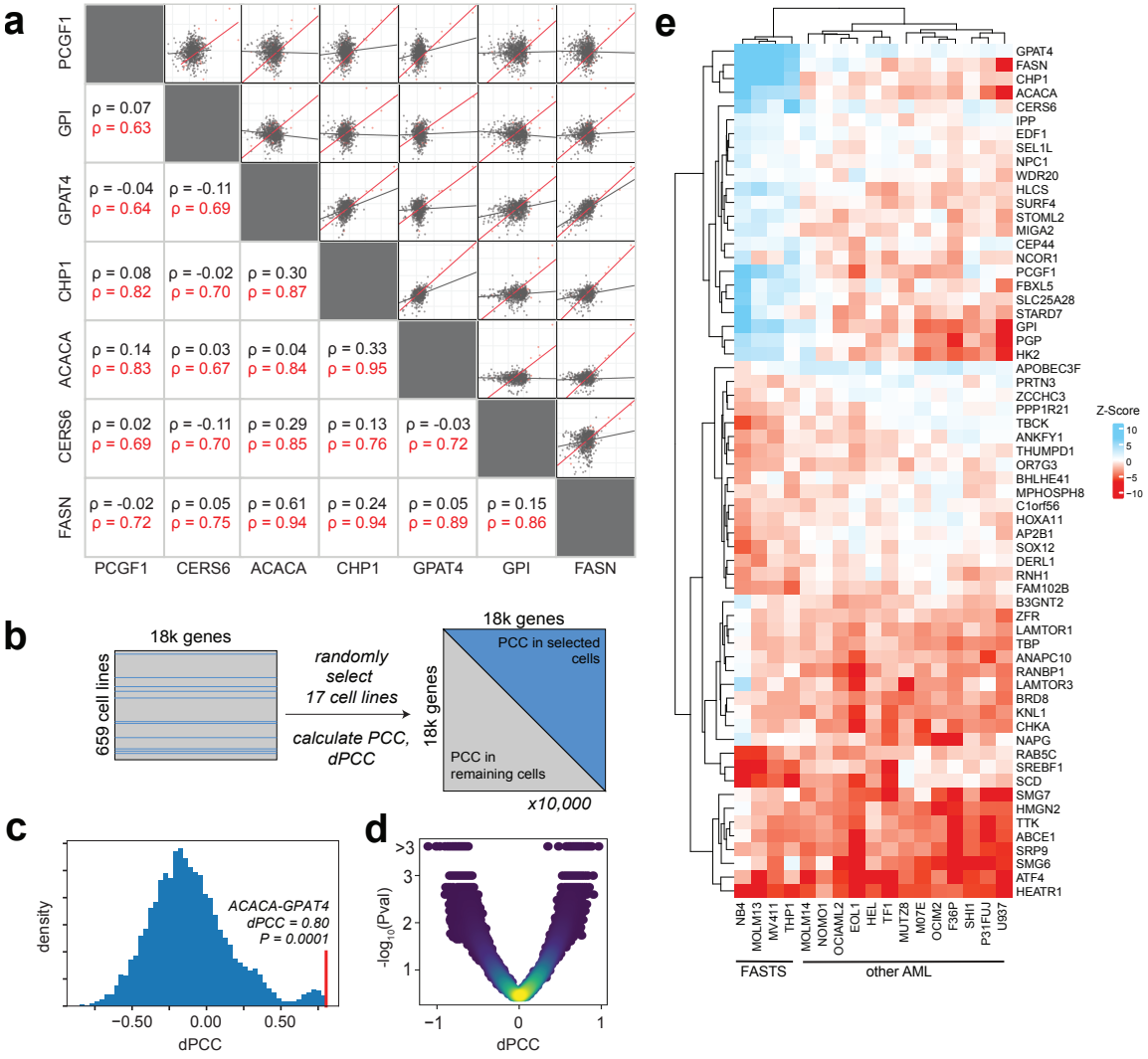
a
PCGF1
GPI
GPAT4
CHP1
ACACA
CERS6
FASN
ρ = 0.07
ρ = 0.63
ρ = -0.04
ρ = 0.64
ρ = -0.11
ρ = 0.69
ρ = 0.08
ρ = 0.82
ρ = -0.02
ρ = 0.70
ρ = 0.30
ρ = 0.87
ρ = 0.14
ρ = 0.83
ρ = 0.03
ρ = 0.67
ρ = 0.04
ρ = 0.84
ρ = 0.33
ρ = 0.95
ρ = 0.02
ρ = 0.69
ρ = -0.11
ρ = 0.70
ρ = 0.29
ρ = 0.85
ρ = 0.13
ρ = 0.76
ρ = -0.03
ρ = 0.72
ρ = -0.02
ρ = 0.72
ρ = 0.05
ρ = 0.75
ρ = 0.61
ρ = 0.94
ρ = 0.24
ρ = 0.94
ρ = 0.05
ρ = 0.89
ρ = 0.15
ρ = 0.86
PCGF1
CERS6
ACACA
CHP1
GPAT4
GPI
FASN
b
18k genes
659 cell lines
randomly select 17 cell lines
calculate PCC, dPCC
18k genes
18k genes
PCC in selected cells
PCC in remaining cells
x10,000
c
density
ACACA-GPAT4
dPCC = 0.80
P = 0.0001
−0.50
0.00
0.50
dPCC
d
>3
3
2
1
-log10(Pval)
−1
0
1
dPCC
e
GPAT4
FASN
CHP1
ACACA
CERS6
IPP
EDF1
SEL1L
NPC1
WDR20
HLCS
SURF4
STOML2
MIGA2
CEP44
NCOR1
PCGF1
FBXL5
SLC25A28
STARD7
GPI
PGP
HK2
APOBEC3F
PRTN3
ZCCHC3
PPP1R21
TBCK
ANKFY1
THUMPD1
OR7G3
BHLHE41
MPHOSPH8
C1orf56
HOXA11
AP2B1
SOX12
DERL1
RNH1
FAM102B
B3GNT2
ZFR
LAMTOR1
TBP
ANAPC10
RANBP1
LAMTOR3
BRD8
KNL1
CHKA
NAPG
RAB5C
SREBF1
SCD
SMG7
HMGN2
TTK
ABCE1
SRP9
SMG6
ATF4
HEATR1
Z-Score
10
5
0
−5
−10
NB4
MOLM13
MV411
THP1
MOLM14
NOMO1
OCIAML2
EQL1
HEL
TF1
MUT28
M07E
OCIM2
F36P
SHI1
P31FUJ
U937
FASTS
other AML

536

537

538 **Figure 3. Differential network analysis of fatty acid synthesis module**. (a) Among genes in
539 the FAS module, Pearson correlation coefficients of shuffled Z score profiles are substantially
540 higher in AML cells (red) than in other cells (gray). (b) Significance testing of differential PCC
541 (dPCC) involves quality filtering of Avana data (n=659 cell lines, including 17 AML cell lines),
542 building a null distribution by randomly selecting 17 cell lines, and calculating PCC between all
543 gene pairs in the selected cells and the remaining cells. (c) After 1,000 repeats, a null distribution
544 is generated for each pair, and a two-sided P-value is calculated for the observed AML-vs-other
545 dPCC. (d) Volcano plot of dPCC vs. P-value for all genes in the Co-PS cluster. (e) Heatmap of
546 mixed Z score for 17 AML cell lines in selected genes with high |mixed Z| and high |dPCC|.
547 Clustering of cell lines indicates the putative Fatty Acid Synthesis/Tumor Suppressor (FASTS)
548 subtype.
549

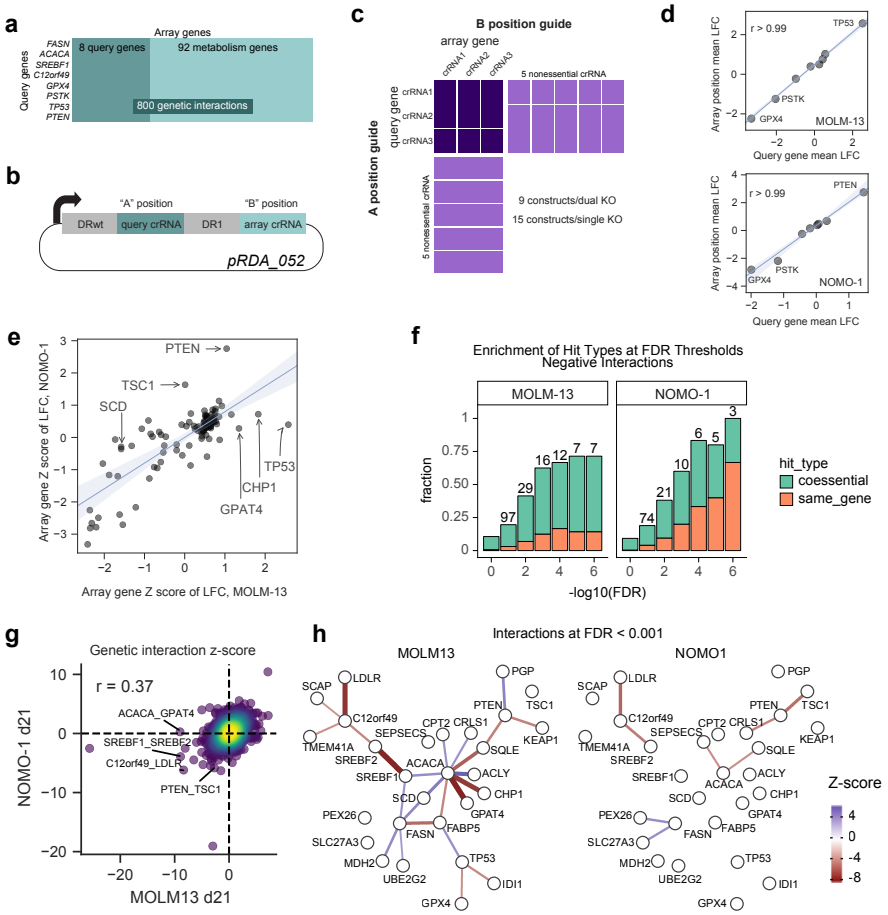
a
Array genes
Query genes
FASN
ACACA
SREBF1
C12orf49
GPX4
PSTK
TP53
PTEN
8 query genes
92 metabolism genes
800 genetic interactions
b
"A" position
"B" position
DRwt
query crRNA
DR1
array crRNA
pRDA_052
c
B position guide
array gene
crRNA1
crRNA2
crRNA3
5 nonessential crRNA
A position guide
query gene
9 constructs/dual KO
15 constructs/single KO
d
r > 0.99
TP53
PSTK
GPX4
MOLM-13
Array position mean LFC
Query gene mean LFC
PTEN
NOMO-1
e
PTEN
TSC1
SCD
TP53
CHP1
GPAT4
Array gene Z score of LFC, NOMO-1
Array gene Z score of LFC, MOLM-13
f
Enrichment of Hit Types at FDR Thresholds
Negative Interactions
MOLM-13
NOMO-1
fraction
-log10(FDR)
hit_type
coessential
same_gene
g
Genetic interaction z-score
r = 0.37
ACACA_GPAT4
SREBF1_SREBF2
C12orf49_LDLR
PTEN_TSC1
NOMO-1 d21
MOLM13 d21
h
Interactions at FDR < 0.001
MOLM13
NOMO1
Z-score

Figure 4

552 **Figure 4. Genetic interactions reveal a rewired lipid biosynthesis pathway in FASTS cells**.
553 (a) Genetic interaction screen targets 8 query genes, selected from FASTS cluster and dPCC
554 analysis, and 100 array genes sampling lipid metabolism pathways, for a total of 800 pairwise
555 knockouts. (b) Library design uses a dual-guide enCa12a expression vector which targets the
556 query gene in the "A" position and array gene in the "B" position. (c) Overall library design includes
557 three crRNA/gene plus control crRNA targeting nonessential genes. Single-knockout constructs
558 (target gene paired with nonessential controls) allow accurate measurement of single knockout
559 fitness. (d) Considering single knockout fitness of query genes in the "A" and "B" position of the
560 crRNA expression vector shows no position effects in the two cell lines screened (MOLM13,
561 NOMO1). LFC, log fold change. (e) Single knockout fitness (Z-score of mean LFC) is highly
562 consistent between MOLM13 and NOMO1, but reveals background-specific PS genes. (f)
563 Enrichment among GI for coessential and self-interacting genes. Self-interactions among genes
564 that show single knockout fitness phenotypes are expected, reflecting quality of GI observations.
565 (g) Global comparison of MOLM13, NOMO1 genetic interaction Z scores. (h) Network view of
566 interactions in each background shows rewiring in MOLM13 FASTS cells.
567

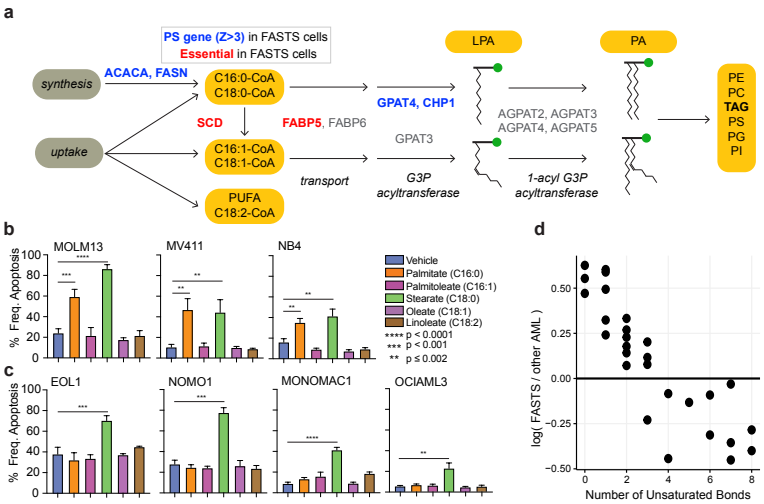
a
PS gene (Z>3) in FASTS cells
Essential in FASTS cells
synthesis
ACACA, FASN
uptake
C16:0-CoA
C18:0-CoA
SCD
C16:1-CoA
C18:1-CoA
PUFA
C18:2-CoA
FABP5, FABP6
transport
GPAT4, CHP1
GPAT3
G3P
acyltransferase
LPA
AGPAT2, AGPAT3
AGPAT4, AGPAT5
1-acyl G3P
acyltransferase
PA
PE
PC
TAG
PS
PG
PI
b
MOLM13
MV411
NB4
% Freq. Apoptosis
Vehicle
Palmitate (C16:0)
Palmitoleate (C16:1)
Stearate (C18:0)
Oleate (C18:1)
Linoleate (C18:2)
**** p < 0.0001
*** p < 0.001
** p ≤ 0.002
c
EOL1
NOMO1
MONOMAC1
OCIAML3
d
log(FASTS / other AML)
Number of Unsaturated Bonds

Figure 5

571 **Figure 5. FASTS cells are sensitive to saturated FA**. (a) Schematic of the fatty acid/glycerolipid
572 synthesis pathway. Blue, PSG in FASTS cells. Red, essential genes. Pathway analysis suggests
573 saturated fatty acids are a critical node. (b) Apoptosis of FASTS cells in response to media
574 supplemented with 200 μm fatty acids. All three cell lines show marked sensitivity to palmitate.
575 (c) Apoptosis of other AML cells in response to fatty acids shows no response to palmitate. (d)
576 Triacylglycerol (TAG) species metabolite differences. The x axis represents the median difference
577 of log10 normalized peak area of the metabolite in FASTS cells vs all other AML cells. The y axis
578 represents the number of saturated bonds present. Each dot represents a unique metabolite.
579

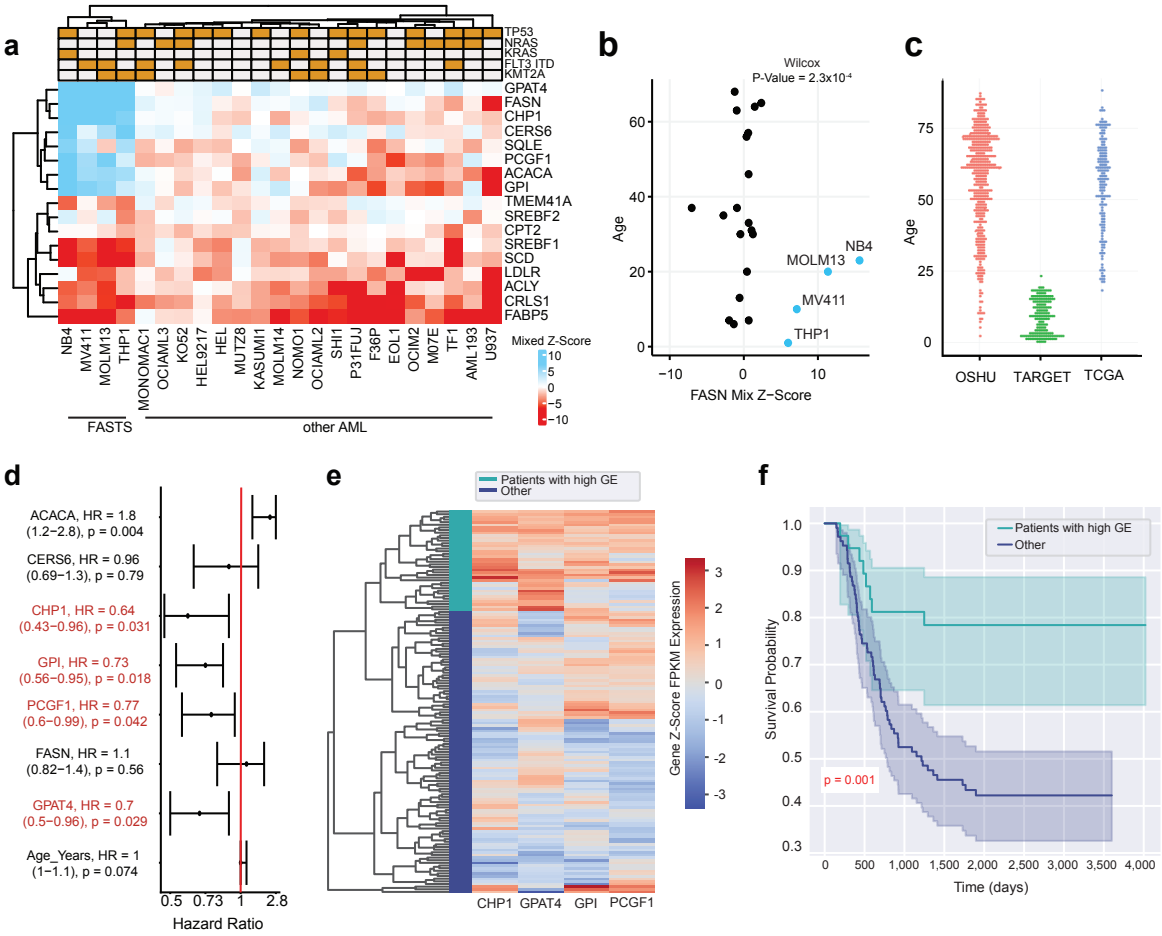
a
TP53
NRAS
KRAS
FLT3 ITD
KMT2A
GPAT4
FASN
CHP1
CERS6
SQLE
PCGF1
ACACA
GPI
TMEM41A
SREBF2
CPT2
SREBF1
SCD
LDLR
ACLY
CRLS1
FABP5
NB4
MV411
MOLM13
THP1
MONOMAC1
OCIAML3
KO52
HEL9217
HEL
MUTZ8
KASUMI1
MOLM14
NOMO1
OCIAML2
SHI1
P31FUJ
F36P
EOL1
OCIM2
M07E
TF1
AML193
U937
FASTS
other AML
Mixed Z-Score
b
Wilcox
P-Value = 2.3x10-4
Age
FASN Mix Z−Score
NB4
MOLM13
MV411
THP1
c
Age
OSHU
TARGET
TCGA
d
ACACA, HR = 1.8
(1.2−2.8), p = 0.004
CERS6, HR = 0.96
(0.69−1.3), p = 0.79
CHP1, HR = 0.64
(0.43−0.96), p = 0.031
GPI, HR = 0.73
(0.56−0.95), p = 0.018
PCGF1, HR = 0.77
(0.6−0.99), p = 0.042
FASN, HR = 1.1
(0.82−1.4), p = 0.56
GPAT4, HR = 0.7
(0.5−0.96), p = 0.029
Age_Years, HR = 1
(1−1.1), p = 0.074
Hazard Ratio
e
Patients with high GE
Other
Gene Z-Score FPKM Expression
CHP1
GPAT4
GPI
PCGF1
f
Patients with high GE
Other
Survival Probability
p = 0.001
Time (days)

580

581

582

583 **Figure 6. Prognostic signature of FAS module**. (a) Heatmap of mixed Z scores for genes
584 implicated in the genetic interaction network. Top, common AML lesions. (b) Mixed Z-score of
585 FASN in AML cell lines vs. age of patient from which cell lines were derived. Blue, FASTS cells.
586 (c) Age distribution of AML patients in three public tumor genomics cohorts. (d) Hazard ratios
587 (95% CI; univariate Cox proportional hazards test) for expression of genes in (a), using genomics
588 and survival data from TARGET. (e) Hierarchical clustering of gene expression in TARGET, using
589 the four genes with negative HR. Green, high expression cluster. Blue, others. (F) Kaplan-Meier
590 survival analysis of AML patients in TARGET, comparing patients in high expression cluster vs.
591 others.
592

593 ***Supplementary Materials and Methods***

594

595 **Code Availability**

596

597 Mixed Z-scoring, analysis using scoring metric, co-occurrence network, and survival analysis was
598 conducted in R version 4.0.4[74,75]. dPCC correlation analysis, including empirical calculations were
599 conducted in Python 3.8.2[76], using the packages SciPy[77], NumPy[78], Matplotlib[79], and pandas[80].
600 Code is made available at: https://github.com/hart-lab/tsg_crispr_screen_survey/. R packages
601 tidyverse[81], data.table[82], and knitr[83–85] were used for figure generation, data manipulation, and
602 general R functions; mixtools[86], permute[87], and PRROC[88,89] were used for data simulations
603 present in figures and evaluation; biomaRt[90,91], and org.Hs.eg.db[92] were used in integrating data
604 types; cowplot[93], ggbeeswarm[94], annotate[95], RColorBrewer[96], ComplexHeatmap[97], gplots[98],
605 ggpubr[99], grid[75], circlize[100], ggthemes[101], ggExtra[102], patchwork[103], and ggplot2[104], were used for
606 figure aesthetics and generation. R packages survival[105,106] and survminer[107] were used for
607 survival analysis and figure generation. Analysis related to Kaplan Meier and patient
608 stratification was done in python version 3.8.5[108] using the packages pandas[80], numpy[78], and
609 scipy[77] for statistical functions and data manipulation, seaborn[109], plotly[110], and matplotlib[79]
610 for figure aesthetics and generation, and lifelines[111] for both statistical analysis and figure
611 generation.

612

613

614 Analysis of enCas12a multiplex genetic screens was conducted in R 4.0.0 and Python 3.8.3[112].
615 Code for this analysis is available at https://github.com/PeterDeWeirdt/FASTS. R packages
616 tidyverse[81] and tidygraph[113] were used for data manipulation and ggraph[114] was used for graph
617 visualization. Python packages SciPy[77], NumPy[78], Matplotlib[79], pandas[80], statsmodels[115],
618 plotnine[116] were used for analysis and visualization. The Custom package gnt[117] was used to
619 calculate genetic interaction scores and gpplot[118] was used to generate point density plots.

620

621 **Processing DepMap Screen and CCLE Genomics Data**

622

623 Raw read count data and a map of guide RNAs were downloaded from the DepMap database
624 (www.depmap.org)[10,48] and Project Score database (https://depmap.sanger.ac.uk/)[13]. Avana data
625 version 2020q4[49] was used for this analysis. To avoid genetic interaction effects, we discarded
626 sgRNAs targeting multiple protein coding genes annotated as public or update pending in The

627 Consensus Coding Sequence (CCDS, release 22)[119]. Gene names in the guide RNA maps of
628 Avana and Project Score were updated using human gene information obtained from ncbi ftp.
629 Then, read count data for each replicate was passed through CRISPRcleanR[120] with location
630 information of sgRNAs for the Avana CRISPR library based on GENCODE[121] to correct depletion
631 effects caused by copy-number amplification. Following this correction, each guide's $\log_2$ fold-
632 change was calculated. For Project Score data, we used only the gene location information of KY
633 library v1.0 which is built in CRISPRcleanR. Normalized TPM RNA-seq data, copy number data,
634 and mutation annotations for CCLE[69] cells were also downloaded from DepMap. Ensembl gene
635 id in RNA-seq data was converted to gene symbol using cross reference downloaded from
636 Emsembl Biomart[122].
637
638 **Mixed Z-Score Metric**
639
640 Mixed z-score metric was generated using R version 4.0.4 base stat packages[75] and the
641 mixtools[86] normalmixEM function. To calculate the mixed z-score, individual guide $\log_2$ fold-
642 changes for each cell line were passed through the default settings of the normalmixEM function
643 to fit two distinction normal distributions. Of the 808 cell lines passed through this analysis, 805
644 cell lines were able to converge with two distinction normal distribution following 1,000 iterations.
645 The calculated mean and standard deviation of the higher (more positive) distribution were
646 recorded. Along with the uncorrected original gene $\log_2$ fold-change, was used to calculate the
647 corresponding mixed z-score. The original and mixed Z-score formula is as follows:

648 $$Mixed\ Gene\ Z - Score = \frac{x - \mu_{high}}{\sigma_{high}}$$

649 Where x is the original gene $\log_2$ fold-change, μ_{high} is the average of the more positive fitted
650 distribution, and σ_{high} is the standard deviation of the more positive fitted distribution. This metric
651 was calculated for the DepMap 2020q4[49] screen set, and the Sanger's DepMap[13] screen set for
652 **Supplementary Figure 3**.
653
654 **Comparisons of Fitness Scoring Metrics**
655
656 The following describes our comparative analysis of screening algorithms observed in
657 **Supplementary Figure 1**. JACKS[43] and BAGEL[41,42,123], software was downloaded from their
658 corresponding GitHub official distribution sites: https://github.com/felicityallen/JACKS, and
659 https://github.com/hart-lab/bagel. We ran JACKS and BAGEL with raw fold change data of

660 DepMap 2020q4 version[49], gene guide map and replicate information. We obtained DepMap
661 2020q4 CERES scores from 'dependency_score.csv' downloaded from DepMap depository.
662 Ranking was performed per screen and based on mean $\log_2$ fold-change values per gene.
663
664 We used the cancer gene census (CGC) list from COSMIC[45,46] to compare fitness methods that
665 can detect proliferation suppressor activity. Tumor suppressor genes (TSGs) from CGC represent
666 a gene set of well-known proliferation suppressors. We separated the CGC gene list in two gene
667 sets, genes with any tumor suppressor role in cancer representing true positive proliferation
668 suppressor observations, and genes with any oncogene role in cancer representing false
669 positives. Additionally, we added reference non-essential genes[7,47] to the false positive list as
670 these genes are not expected to demonstrate any phenotype. With these compiled lists, we
671 evaluated each metric's fitness scores, to see which metric would best separate the true and false
672 positive gene lists. The R package PRROC was used for fitness scoring evaluation[88,89].
673
674 **Direct Proliferation Suppressor Comparisons of Avana and Sanger Screen Datasets**
675
676 The CRISPRcleanR[120] corrected fold-change Sanger screen set[13] was pushed through identical
677 pipelines used to calculate the mixed z-score metric. Quality analysis of the mixed z-score metric
678 for both data sets was pushed using identical gene sets described in the "Comparisons of Fitness
679 Scoring Metrics" section. This analysis was restricted to only overlapping cell lines, 186 total, in
680 both datasets.
681
682 The fitness enhancement introduced by PSG knockout, relatively weak compared to severe
683 defects from essential gene knockout, often precludes detection in a shorter experiment. In the
684 example F5 cell line (**Figure 1a**), a 2.5-fold change over a 21-day time course corresponds to a
685 fitness increase of only ~12% for rapidly growing cells, or a doubling time decrease from 24 to 21
686 hours. In a 14-day experiment, this increased proliferation rate would result in an observed log
687 fold change of only ~1.7, within the expected noise from genes with no knockout phenotype. This
688 is explained in detail as follows:
689
690 ***Theoretical Fold-Change and Growth Rate Quantification:*** To assess hypothetical differences
691 of proliferation suppressor fitness scoring metrics based on standard sampling times of screen
692 collection taken from the Sanger and Avana databases[10,11,13,48], we calculated theoretical cell

population differences of wild-type and knocked out proliferation suppressor cell lines. The following formula can be used to calculate cell populations based on doubling rate per day:

$$X_f = X_i * 2^{k*t}$$

In this formula X_f is the final population number of cells, X_i is the initial population of cells, k is doubling time of the cells (in days), and t is time in days. In order to compare cells we can assume that these formulas are consistent with both wild-type cells and knocked out proliferation suppressor cells. With, knocked out proliferation suppressor cells the assumption is that these cells would grow faster compared to wild-type conditions and thus $k_{ps} > k_{wt}$, where k_{ps} is the growth rate for proliferation suppressor knocked out cells, and k_{wt} is the growth rate of wild type cells. These two independent growth rates are related as:

$$k_{ps} = k_{wt} + \Delta k$$

Δk represents the change in growth rate resulting from genetic knockout, and is assumed to be positive. The growth rate formula for wild-type and proliferation suppressor cells is thus:
$X_{wt} = X_i * 2^{k_{wt}*t}$, $X_{ps} = X_i * 2^{(k_{wt}+\Delta k)*t}$

We then solved for Δk, with $Log_2(X_{ps}/X_{wt})$ as $Log_2(FC)$, representing the fold-change difference between the cell populations at time t:

$$Log_2FC = Log_2\left(\frac{X_{ps}}{X_{wt}}\right)$$

$$Log_2FC = Log_2\left(\frac{X_i * 2^{(k_{wt}+\Delta k)*t}}{X_i * 2^{k_{wt}*t}}\right)$$

$$Log_2FC = Log_2\left(\frac{2^{(k_{wt}+\Delta k)*t}}{2^{k_{wt}*t}}\right)$$

$$Log_2FC = ((k_{wt} + \Delta k) * t) - (k_{wt} * t)$$

$$Log_2FC/t = k_{wt} + \Delta k - k_{wt}$$

$$Log_2FC/t = \Delta k$$

For a representative *Log₂(FC)* of 2.5, which represents a sizable gain in fitness from a knocked-out proliferation suppressor, and *t* = 21 days, representing the time in which the Avana screens were sampled, we calculated Δ*k*:

$$\Delta k = \frac{2.5}{21} = 0.12$$

Using the calculated Δ*k* at 0.12, we can calculate the hypothetical *Log₂(FC)* that would be expected at *t* = 14 days, representing the time in which the Sanger screens were sampled:

$$Log_2FC = \Delta k * t$$

$$Log_2FC = 0.12 * 14 = 1.7$$

The resulting theoretical measurements demonstrate that Δ*k* can be identical between two samples, however the time in which the sample was taken will influence the ratio between the two measured cell populations. Taken together, this demonstrates that samples at shorter time points will demonstrate smaller quantified population size differences between wild-type and proliferation suppressor knocked out cells compared to samples taken at longer time points.

Proliferation Suppressor Co-Occurrence Network

The co-occurrence network was developed based on FDR-corrected P-values from Fisher exact tests of all gene by gene comparisons that were identified as a proliferation suppressor more than once (584 genes total). Parallel processing, Fisher's exact test, Benjamini & Hochberg FDR p-value adjustment were done using base R stat packages[75]. **Figure 2a** was created with heatmap.2 function from the R gplots[98] package, with the dendrogram created through base R[75] functions of euclidean distance, and complete agglomeration methods clustering of the Fisher's exact test score between gene pairs. Smaller heatmaps displayed in **Figure 2c** were made using the R ComplexHeatmap library[97]. Network visualization was completed using Cytoscape[124].

757 Network creation followed the corresponding steps; **1)** Identify all proliferation suppressor
758 observations at a 10% FDR threshold (Z >= 3.83). **2)** Filter for gene proliferation suppressor
759 observations that occurred at least 2 or more times, selecting for a total of 584 out of 18,111
760 genes available (3.2% total available genes); **3)** Create a binary (1 = proliferation suppressor, 0
761 = not proliferation suppressor) matrix of all 584 genes in all cell lines; **4)** Conducted Fisher's exact
762 test of every possible 2 x 2 contingency table of the 584 selected genes (n= 170,236 tests); and
763 **5)** Adjust the corresponding p-values to FDR values, using a cutoff of 0.001 (0.1% FDR) to define
764 edges. By assessing gene edges through Fisher exact-tests, we observe gene associations that
765 are based on the relative proportion of co-occurrences between two genes.
766
767
768 **Proliferation Suppressor Network Enrichment**
769
770 To test network enrichment of observed edges (**Supplementary Figure 4a**), we took 10,000
771 random samples of 462 (total number of edges in the co-occurrence network) gene pairs from the
772 170,236 available all by all gene pair Fisher's exact test set. We then compared each sample to
773 see the frequency of gene pairs observed to have some interaction within HumanNet[61], excluding
774 genetic interactions observed solely in the co-essentiality network component[21] (generated from
775 the same data) to prevent circularity. Additionally, we compared our selected mixed Z-Score cutoff
776 against other various Z-Score cutoffs to ensure that we observed appropriate edge representation
777 from HumanNet (**Supplementary Figure 4b**). Networks were made using identical pipelines and
778 Fisher's exact test set cutoffs with Z-Score cutoffs between 3 and 8 at 0.2 increments.
779
780 **Differential Pearson Correlation Coefficient Analysis**
781
782 Differential Pearson correlation coefficient (dPCC) analysis was conducted to identify genetic
783 fitness distinctions between AML cells and all other cells (**Figure 3**). Initial correlations (**Figure**
784 **3a**) of FAS cluster genes, PCGF1, CERS6, GPI, FASN, CHP1, GPAT4, and ACACA were
785 calculated with R version 4.0.4 base stat packages[75] and plotted in ggplot2[104].
786
787 Following this observation, a follow up dPCC analysis was conducted on the FASTS cluster genes
788 to assess dPCC quality. Cell line screens with low quality (Cohen's D < 2.5 or recall of known
789 core essential genes < 60%) were excluded, leaving 659 cell lines. Following this filtering step,
790 two gene-by-gene correlation matrices were calculated. The first correlation matrix calculated all

791 gene by gene pairs in only the available AML cell lines (n=17). The second matrix calculated all
792 gene by gene pairs in the remaining 642 cell lines. The dPCC matrix is therefore the AML
793 correlation matrix minus the non-AML correlation matrix.
794
795 Each gene-pair has a unique joint distribution of mixed Z scores; thus, the significance of each
796 dPCC score must be calculated individually. To do this, we generated null distributions for dPCC
797 for each gene pair. We took random selections without replacement of 17 cell lines (matching the
798 n of AML cells), calculated all gene by gene pairwise correlations within this selection and within
799 the remainder, and calculated dPCC. We repeated this sampling and calculation 1,000 times to
800 generate a unique null distribution of dPCC for each gene pair and calculated an appropriate P-
801 value for the observed dPCC above (right tailed for positive dPCC, left tailed for negative dPCC).
802
803 Genes which showed signficant knockout phenotype (|mixed Z| > 5) and AML-specific change in
804 correlation (dPCC P<0.001) with a gene in the connected clique in the co-occurrence cluster
805 (*CHP1, GPAT4, ACACA, FASN, GPI, CERS6, PCGF1*) were selected for further analysis (**Figure**
806 **3e**). **Figure 3e** was made using the R ComplexHeatmap library[97]. **Figure 3c-d** plots were made
807 using the Python package Matplotlib[79].
808
809 **Cell culture for Genetic Screens**
810
811 MOLM13 and NOMO1 cells screened with the Cas12a-mediated genetic interaction library at the
812 Broad Institute were obtained from the Cancer Cell Line Encyclopedia.
813
814 All cell lines were routinely tested for mycoplasma contamination and were maintained without
815 antibiotics except during screens, when the media was supplemented with 1%
816 penicillin/streptomycin. Cell lines were kept in a 37 °C humidity-controlled incubator with 5.0%
817 carbon dioxide and were maintained in exponential phase growth by passaging every 2-3 days.
818 The following media conditions and doses of polybrene, puromycin, and blasticidin, respectively,
819 were used:

820 MOLM13: RPMI + 10% FBS; 8 μg mL^{-1}; 4 μg mL^{-1}; 8 μg mL^{-1}

821 NOMO1: RPMI + 10% FBS; 8 μg mL^{-1}; 1 μg mL^{-1}; 8 μg mL^{-1}
822
823 **Pooled screens**

824

825 Cell lines stably expressing enCas12a (pRDA_174, Addgene 136476) were transduced with
826 guides cloned into the pRDA_052 vector (Addgene 136474) in two cell culture replicates at a low
827 MOI (~0.5). Transductions were performed with enough cells to achieve a representation of at
828 least 750 cells per guide construct per replicate, taking into account a 30–50% transduction
829 efficiency. Throughout the screen, cells were split at a density to maintain a representation of at
830 least 1000 cells per guide construct, and cell counts were taken at each passage to monitor
831 growth. Puromycin selection was added 2 days post-transduction and was maintained for 5 days.
832 14 days and 21 days after transduction, cells were pelleted by centrifugation, resuspended in
833 PBS, and frozen promptly for genomic DNA isolation.
834
835
836 **Genomic DNA isolation and PCR**
837
838 Genomic DNA (gDNA) was isolated using the KingFisher Flex Purification System with the Mag-
839 Bind® Blood & Tissue DNA HDQ Kit (Omega Bio-Tek #M6399-01) as per the manufacturer's
840 instructions. The gDNA concentrations were quantitated by Qubit. For PCR amplification, gDNA
841 was divided into 100 µL reactions such that each well had at most 10 µg of gDNA. Per 96 well
842 plate, a master mix consisted of 144 µL of 50x Titanium Taq DNA Polymerase (Takara), 960 µL
843 of 10x Titanium Taq buffer, 768 µL of dNTP (stock at 2.5mM) provided with the enzyme, 48 µL of
844 P5 stagger primer mix (stock at 100 µM concentration), 480 µL of DMSO, and 1.44 mL water.
845 Each well consisted of 50 µL gDNA plus water, 40 µL PCR master mix, and 10 µL of a uniquely
846 barcoded P7 primer (stock at 5 µM concentration).
847
848 PCR cycling conditions: an initial 1 min at 95 °C; followed by 30 s at 94 °C, 30 s at 53 °C, 30 s at
849 72 °C, for 28 cycles; and a final 10 min extension at 72 °C. PCR primers were synthesized at
850 Integrated DNA Technologies (IDT). PCR products were purified with Agencourt AMPure XP
851 SPRI beads according to manufacturer's instructions (Beckman Coulter, A63880).
852
853 Samples were sequenced on a HiSeq2500 Rapid Run flowcell (Illumina) with a custom primer of
854 sequence: 5'-CTTGTGGAAAGGACGAAACACCGGTAATTTCTACTCTTGTAGAT. The first
855 nucleotide sequenced with the primer is the first nucleotide of the guide RNA, which will contain
856 a mix of all four nucleotides, and thus staggered primers are not required to maintain diversity
857 when using this approach. Reads were counted by alignment to a reference file of all possible

858 guide RNAs present in the library. The read was then assigned to a condition (e.g. a well on the
859 PCR plate) on the basis of the 8 nt index included in the P7 primer.
860
861 **Scoring Genetic Interactions**
862
863 To score genetic interactions we used a custom python package, gnt[117], available on the python
864 package index. We use log-fold changes (LFCs) as inputs to the scoring pipeline. We define y_{ij}as
865 the observed LFC of a guide pair $i, j$and $\widehat{y_{ij}}$ as this pair's expected LFC. We then calculate the
866 residual $y_{ij} - \widehat{y_{ij}}$ to generate an interaction score. To define expected LFCs, $\widehat{y_{ij}}$ we fit a linear
867 regression for each guide, i, saying

868 $$\widehat{y_i} = m_i \cdot x + b_i,$$

869 where x is the LFC of each guide individually and m_i and b_i are the fit slope and intercept for
870 guide i (**Supplementary Figure 6b**). We refer to i as the anchor guide and its pairs as target
871 guides. We then Z-score residuals within each anchor guide. This approach is similar to the one
872 taken by Horlbeck *et al.*[33].

873 To aggregate interaction scores at the gene level, we sum the z-scored residuals, z_{ij}, for all
874 constructs i, j targeting the gene pair I, J, fixing I as the anchor gene, and divide by the square
875 root of the number of constructs targeting I, J. We repeat this calculation, fixing Jas the anchor
876 gene. We sum scores for both of these orientations and divide by $\sqrt{2}$ to arrive at a gene level Z-
877 score.

878

879 **Cell Culture for Fatty Acid Response**
880
881 Human cancer cell lines used at MD Anderson were obtained as follows: EOL1, MONOMAC1,
882 NB4, OCIAML3 (DSMZ); MOLM13 and NOMO1 (Fisher); MV411 (ATCC). Identities were
883 confirmed upon receipt and prior to experiments by STR typing (MDACC Characterized Cell Line
884 Core). Absence of mycoplasma was confirmed monthly (Invivogen). All cell lines were grown at
885 37 °C in 5% CO_2 in low attachment flasks (Greiner) and maintained at less than 1M cells ml^{-1}. All
886 but one line were cultured in RPMI-1640 with 25 mM HEPES (Sigma) supplemented with 10%
887 FBS (Sigma), 2 mM Glutamax (Gibco), 1 mM sodium pyruvate (Gibco), 10,000 units ml^{-1} penicillin
888 (Sigma), 10 mg ml^{-1} streptomycin (Sigma) and 100 µg ml^{-1} Normocin (Invitrogen). Complete

889 medium was additionally supplemented with 0.1 mM non-essential amino acids (Gibco) for
890 MONOMAC1.
891
892 **Fatty Acid Solutions**
893
894 Fatty All chemicals were purchased from Sigma (St. Louis, MO). Solutions were prepared
895 according to Luo *et al.*[125] following best practices[126]. Fatty acid stock solutions were prepared in
896 100% ethanol at 50 mM for stearic acid or 200 mM for the rest. Fatty acid free bovine serum
897 albumin (FAF-BSA) was dissolved in tissue culture grade (pyrogen free) water at 1.5 mM (10%
898 w/v), filtered using 0.1 µm PES vacuum unit (Corning) and aliquoted for storage at -20°C. Ethanol
899 stock solutions were diluted to 4 mM in FAF-BSA (molar ratio 2.7:1) and mixed gently at room
900 temperature for 2 hours to facilitate conjugation. A vehicle control was prepared by diluting 100%
901 ethanol in FAF-BSA to match the ethanol concentration in the 4 mM stearic acid solution. Vehicle
902 or 4 mM solutions were aliquoted and stored at -80°C for up to 3 months. After thawing, aliquots
903 were diluted 1:10 with complete medium to 400 µM, stored at 4°C and used within one week.
904
905
906 **Apoptosis Assay**
907
908 Cells were seeded 24 hr prior to treatment in 500 µL complete medium in 24-well low attachment
909 plates (Greiner) at 250,000 cells well^{-1} . Quadruplicate wells received 500 µL FA working solution
910 (400 µM) or vehicle (BSA+EtOH). Cells were treated at 200 µM for 48 hr. Treated cells were
911 transferred to a deep 96 well plate and medium was discarded after centrifugation at 500 x g for
912 5 min. Cells were washed once with 1000 µL D-PBS (Sigma). Next, cells were resuspended in
913 300 µL binding buffer containing annexin-FITC and propidium iodide according to the
914 manufacturer's protocol (BD Biosciences) and transferred to a shallow 96 well V-bottom plate
915 (Corning). After staining for 15 min at room temperature in the dark, cells were washed once with
916 300 µL binding buffer and finally resuspended in 100 µL binding buffer. Unstained and single stain
917 controls were prepared for every cell line in a separate plate. Gates were adjusted such that 99%
918 of unstained singlets fell below each threshold. See **Supplementary Figure 9** for complete gating
919 strategy. Flow cytometry data were collected using a FACSCelesta analyzer equipped with an
920 autosampler (BD Biosciences) and analyzed using FlowJo 10.5.3. Results shown are
921 representative of three independent experiments conducted with sequential passages of each
922 cell line.

923
924
925 **Metabolomics Analysis**
926
927 This section describes the methods used within **Figure 5d** and **Supplementary Figure 7**.
928 Metabolomics data acquired from Supplementary table 1 of Li *et al.*[70] For analysis, normalized
929 data ("1-clean data") and coefficient of variation for each metabolite ("1-CV") was used.
930 Normalized data was filtered to select only AML cells that were present in Avana 2020q4[49] screen
931 set. Following filtering, the median of species present were taken, grouped by whether the
932 measurement was from a FASTS AML or other AML cell line. The difference in median,
933 representing the log ratio, was taken for each metabolite. Metabolites that had differences in
934 medians less than the coefficient of variation were omitted from the plots. Acyl group and number
935 of unsaturated bonds were obtained directly from the provided nomenclature.
936
937 **AML Patient Survival Analysis**
938
939 This section describes the methods used within **Figure 6** and **Supplementary Figure 8 & 10.**
940 The results published here are in part based upon data generated by the Therapeutically
941 Applicable Research to Generate Effective Treatments (TARGET) initiative, phs000218,
942 managed by the NCI. The data used for this analysis are available at dbGaP Study Accession:
943 phs000465.v19.p8. Information about TARGET can be found at
944 http://ocg.cancer.gov/programs/target.
945
946 Genes chosen for analysis were all genes shown to have an interaction with ACACA in **Figure**
947 **4h** and FASN**.** Gene annotations noted in the **Figure 6a** heatmap include any non-silent mutation,
948 copy number loss for TP53 & KMT2A, and copy number gain for KRAS, NRAS, and FLT3. FLT3-
949 ITD annotations were included in the FLT3 annotation row bar. Mutation annotations come from
950 CCLE[69], copy number calls come from the cBioPortal[127,128] database, and FLT-ITD annotations
951 come from the DSMZ catalogue[129].
952
953 TARGET-AML[71] data including age, genetic expression (HTseq FPKM UQ) , time to event, and
954 survival event outcomes, and TCGA[72] patient ages and genetic expression were downloaded
955 directly from the Xena[130] database. The OHSU BeatAML[73] age data was directly downloaded
956 from the Vizome database, and genetic expression data was taken from the original publication.

957 Age of patient derived cell lines were obtained from the Cellosaurus database[131]. Hazard ratios
958 calculated from Cox proportional hazards modeling were done using the R survival[105,106] package.
959 Patient clustering stratification was done with clustering functions from the scipy package[77], using
960 Euclidean clustering and complete linkage settings. This output heatmap (**Figure 6e**) was created
961 using functions from the seaborn[109] package. We identified the patient cluster containing the
962 highest overall expression of CHP1, GPAT4, GPI, PCGF1 from the heatmap using the fcluster
963 function from scipy[77]. **Figure 6f** demonstrates the resulting survival comparison of the two patient
964 clusters and was created with functions from the lifelines[111] package, specifically,
965 KaplanMeierFitter function for the Kaplan Meier curve, and the p-value reflecting the calculated
966 logrank test of the two curves.
967
968 P-values related to schoenfeld tests calculated internally by the survminer package. For TARGET
969 data analysis, patient expression profiles were chosen from primary tumor samples, filtering out
970 samples from recurrent patients (42 such cases). Patient stratification is conducted based on
971 stratifying patient groups into lower genetic expression (patients with genetic expression below
972 the 75th percentile, n = 108), and higher genetic expression (patients with 75th percentile and
973 above, n = 37). Computed hazard ratios for all tested genes within the TARGET cohort all passed
974 the cox proportion hazards assumption (**Supplementary Figure 10**) by failing to reject the
975 schoenfeld test null hypothesis.
976
977 **Supplementary Tables**
978
979 **Table S1. Mixed Distribution Model Z-Score Matrix.** 808 cell line vs 18,111 gene matrix of
980 mixed Z-score derived from log fold-change fitness scores.
981
982 **Table S2. COSMIC TSG PS Statistics.** Statistics of 116 COSMIC TSG genes when observed
983 as a PS, vs other available data points. Includes number of times TSG is observed as a PS
984 gene (count), mean and median TPM expression when observed as a PS gene and additional
985 backgrounds (PS_Mean_Exp, Other_Mean_Exp, PS_Median_Exp, Other_Median_Exp), and
986 non-silent mutation rate as a PS gene and additional backgrounds (PS_mut, Other_mut).

Additionally includes a column of fisher's exact test comparing mutated vs non mutated observations, and a Wilcox test comparing expression levels for each gene.

Table S3. PSG Co-PS network. Network of PSG co-occurrence observations related to **Figures 2c** and **S4c**, including fisher test metrics (p-value and FDR).

Table S4. enCas12a Screen Gene Selection and Rationale.

Table S5. enCas12a Library Design.

Table S6. enCas12a Single Gene Knock-Out Measurements. Z-score of mean Log fold-change.

Table S7. enCas12a Double Gene Knock-Out Measurements. Calculated Log fold-change and corresponding GI Scores for each gene pair.

1004 **Supplementary figure legends**

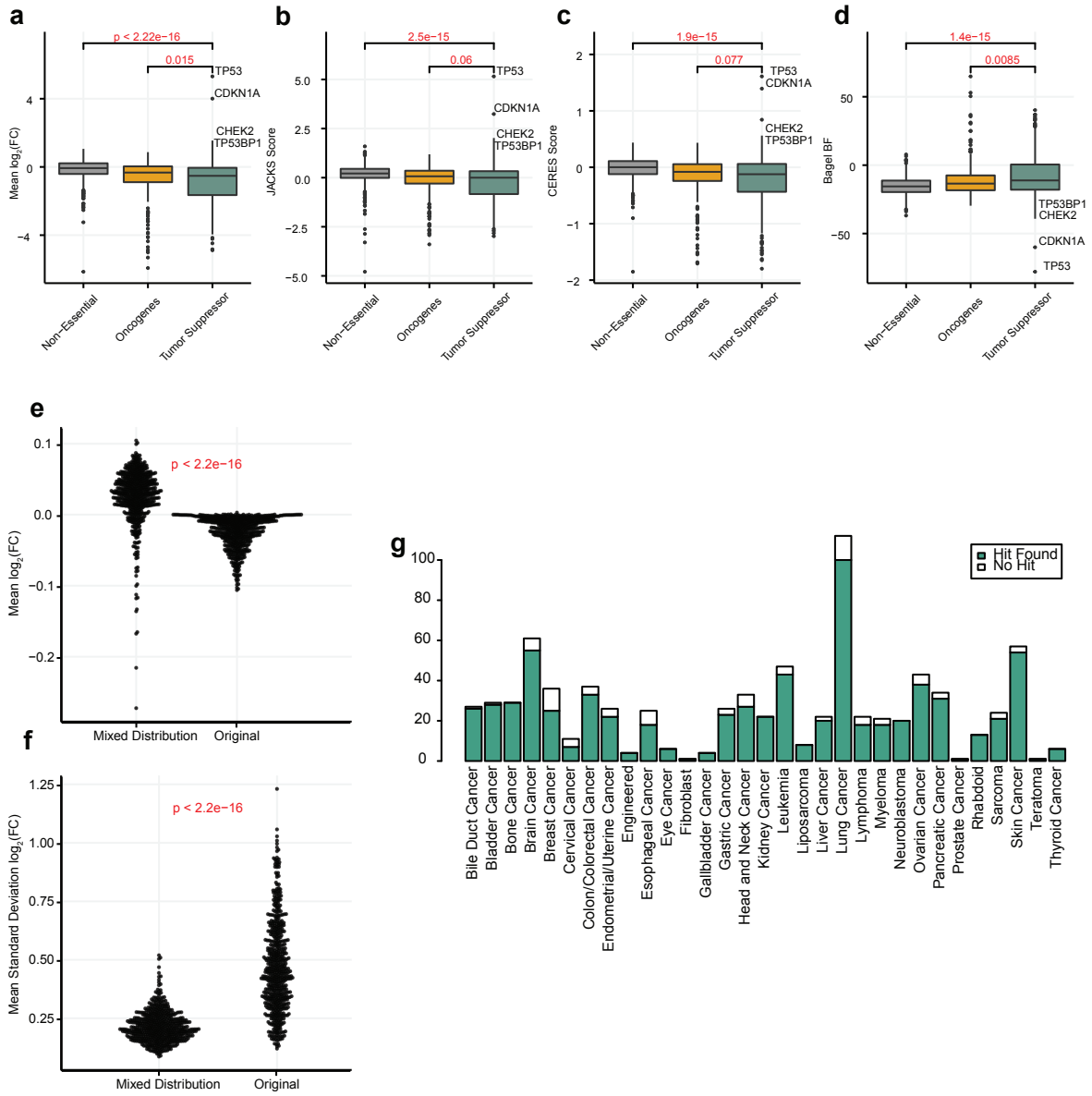

1005

1006

1007

1008 **Figure S1. Discovery of Proliferation Suppressor genes extended**. Fitness scoring
1009 distributions of non-essential genes, and non-overlapping COSMIC defined oncogenes and tumor
1010 suppressor genes; (a) mean log fold-change, (b) JACKS, (c) CERES, and (d) BAGEL. Selected
1011 screen for a-d matches the screen observed in Figure 1a. (e) Distribution of mean log fold-change
1012 of original distribution and mixed distribution . (f) Same (e) with mean standard deviation. (g) Bar
1013 chart by cell line lineage, where at least 1 PS gene at 10% FDR cutoff identified.

1014

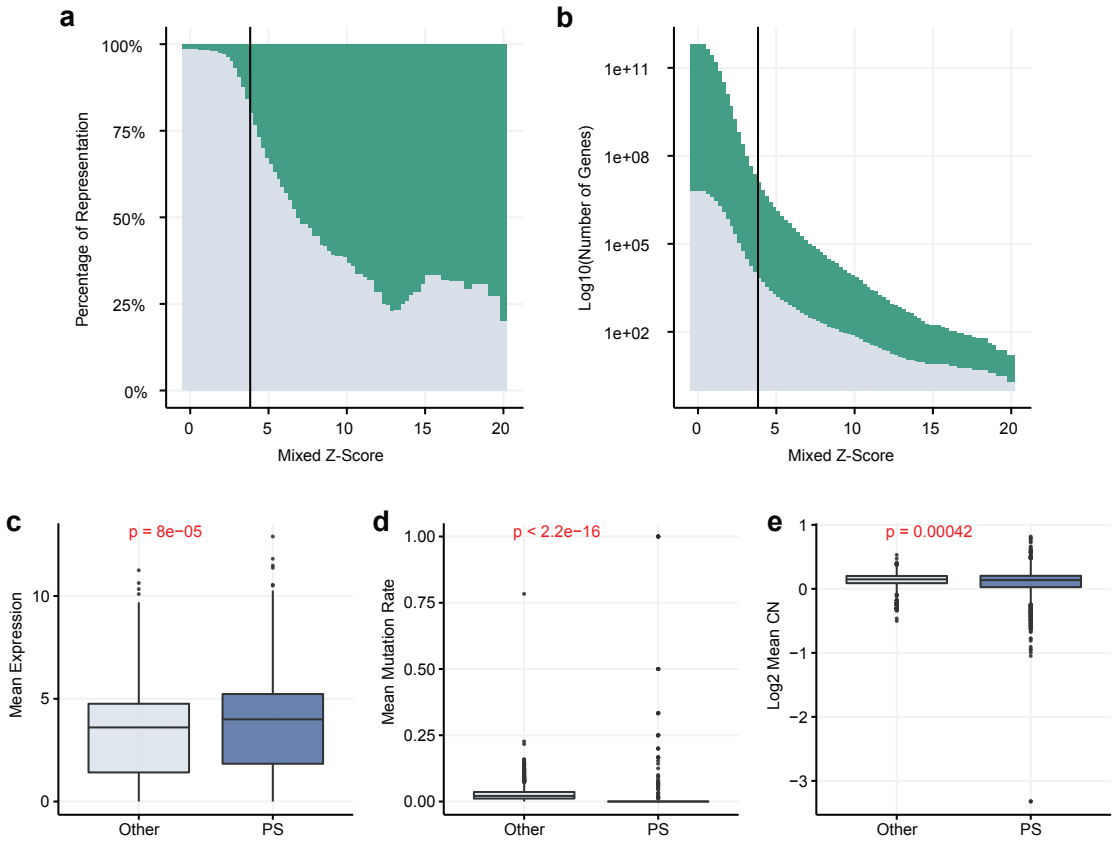
a
100%
75%
50%
25%
0%
Percentage of Representation
0
5
10
15
20
Mixed Z-Score
b
1e+11
1e+08
1e+05
1e+02
Log10(Number of Genes)
0
5
10
15
20
Mixed Z-Score
c
p = 8e−05
Mean Expression
10
5
0
Other
PS
d
p < 2.2e−16
Mean Mutation Rate
1.00
0.75
0.50
0.25
0.00
Other
PS
e
p = 0.00042
Log2 Mean CN
1
0
−1
−2
−3
Other
PS

1015

1016

1017 **Figure S2. Proliferation Suppressor Gene Evidence**. (a) Percent representation of COSMIC
1018 TSG (green) by corresponding label-shuffled Z-score. (b) Same as (a) with log10 y-axis of number
1019 of genes. (c) Mean TPM expression of PSG, grouped by PS observations (blue) vs every other
1020 available observation (gray) in which PSG were not observed as a PS. P value represents the
1021 corresponding Wilcoxon test. (d) same as (c) with mutation rate and (e) copy number.
1022

1023

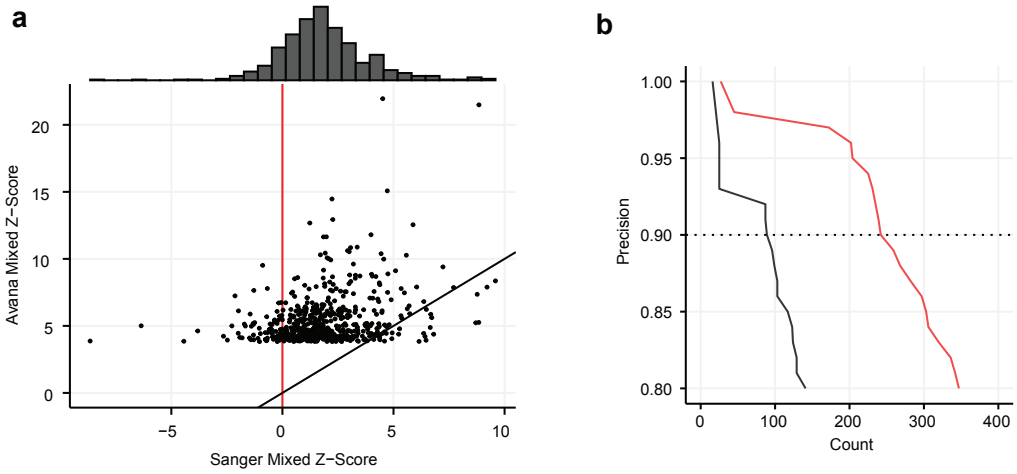

1024

1025

1026 **Figure S3. Avana vs Sanger Genetic Screens Comparison**. (a) Precision vs. recall of mixed

1027 Z-score in matching screens from Avana (red), and Sanger (black). Dashed line, 90% precision

1028 (10% FDR). (b) Avana vs Sanger mixed Z-scores of genes identified as hits in Avana.

1029

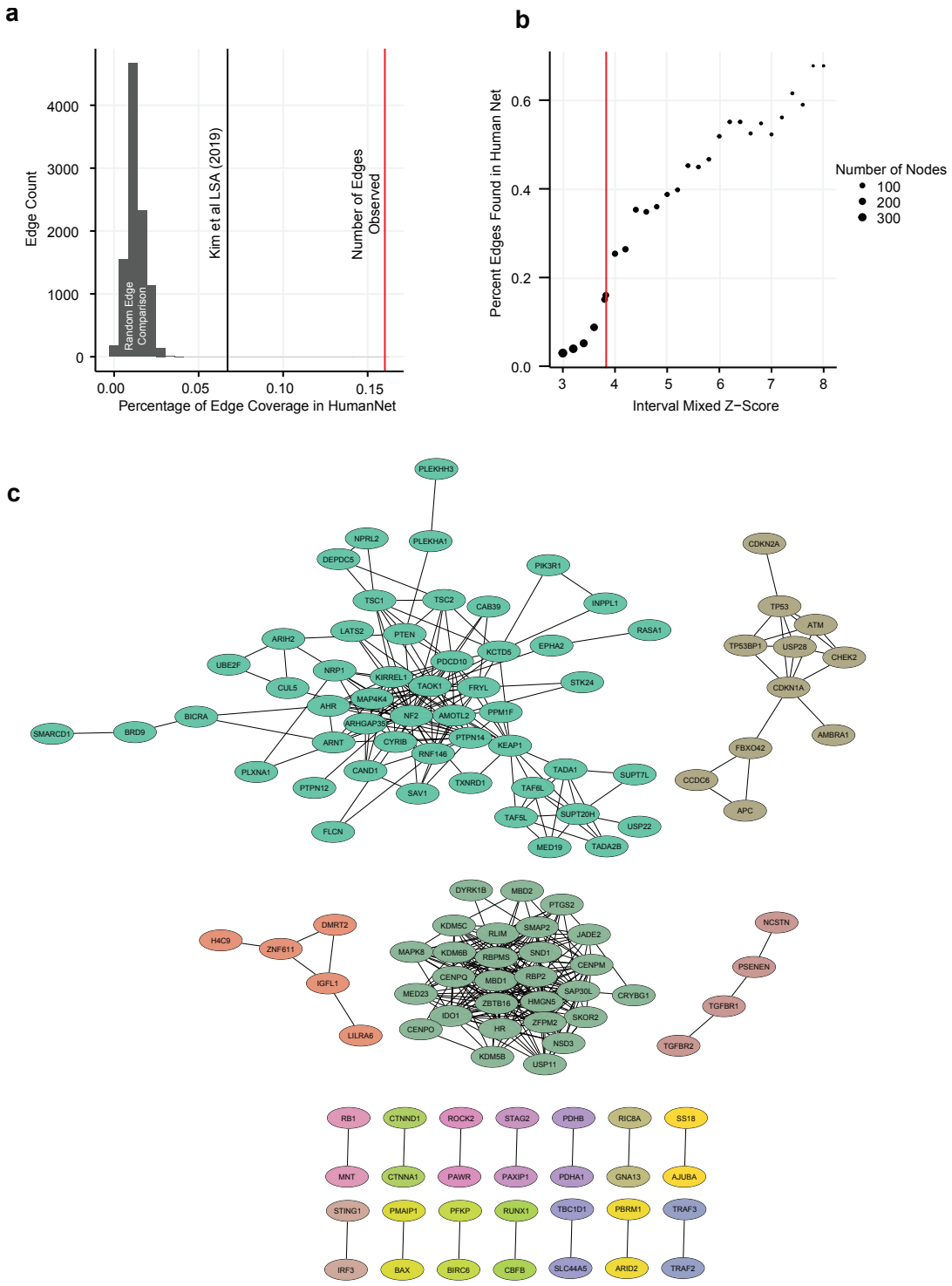
a
Edge Count
4000
3000
2000
1000
0
Random Edge Comparison
Kim et al LSA (2019)
Number of Edges Observed
0.00
0.05
0.10
0.15
Percentage of Edge Coverage in HumanNet
b
Percent Edges Found in Human Net
0.6
0.4
0.2
0.0
3
4
5
6
7
8
Interval Mixed Z−Score
Number of Nodes
100
200
300
c
PLEKHH3
NPRL2
PLEKHA1
DEPDC5
PIK3R1
TSC1
TSC2
CAB39
INPPL1
RASA1
ARIH2
LATS2
PTEN
KCTD5
EPHA2
UBE2F
NRP1
PDCD10
KIRREL1
CUL5
TAOK1
FRYL
STK24
AHR
MAP4K4
BICRA
NF2
AMOTL2
PPM1F
SMARCD1
BRD9
ARHGAP35
ARNT
CYRIB
PTPN14
KEAP1
RNF146
PLXNA1
CAND1
TADA1
SUPT7L
PTPN12
SAV1
TXNRD1
TAF6L
TAF5L
SUPT20H
USP22
FLCN
MED19
TADA2B
CDKN2A
TP53
ATM
TP53BP1
USP28
CHEK2
CDKN1A
AMBRA1
FBXO42
CCDC6
APC
DYRK1B
MBD2
PTGS2
DMRT2
KDM5C
SMAP2
H4C9
ZNF611
RLIM
JADE2
MAPK8
KDM6B
SND1
RBPMS
CENPM
CENPO
RBP2
IGFL1
MBD1
MED23
SAP30L
CRYBG1
ZBTB16
HMGN5
IDO1
SKOR2
ZFPM2
LILRA6
CENPO
HR
NSD3
KDM5B
USP11
NCSTN
PSENEN
TGFBR1
TGFBR2
RB1
CTNND1
ROCK2
STAG2
PDHB
RIC8A
SS18
MNT
CTNNA1
PAWR
PAXIP1
PDHA1
GNA13
AJUBA
STING1
PMAIP1
PFKP
RUNX1
TBC1D1
PBRM1
TRAF3
IRF3
BAX
BIRC6
CBFB
SLC44A5
ARID2
TRAF2

1030

1031

1032

1033 **Figure S4. Co-occurrence of PS genes extended**. (a) Empirical comparison of Co-PS network
1034 edges. Distribution represents random edges between genes identified in the network, and the
1035 percentage of edges identified in HumanNet with coessentiality network removed. Black line
1036 represents the percent of edges identified in the Kim *et al.* coessentiality network. Red line
1037 indicates the actual number of edges the Co-PS contains that are observed in HumanNet with
1038 coessentiality network removed. (b) Percent of edge coverage observed in HumanNet with
1039 coessentiality network removed against Co-PS edge FDR < 0.1%. networks at iterative label
1040 shuffled Z-score cutoffs. Red dot indicates actual cutoff used. (c) Remaining modules from the
1041 Co-PS network not included in Figure 2c.

1042

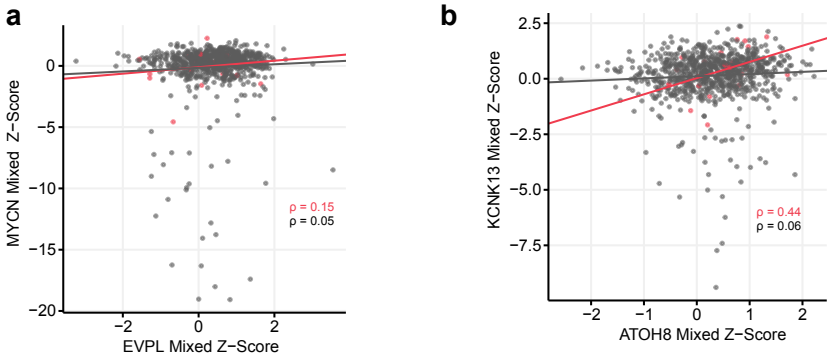
a
MYCN Mixed Z−Score
EVPL Mixed Z−Score
ρ = 0.15
ρ = 0.05
b
KCNK13 Mixed Z−Score
ATOH8 Mixed Z−Score
ρ = 0.44
ρ = 0.06

1043

1044 **Figure S5. Examples of high dPCC resulting from data noise.** (a) EVPL vs MYCN mixed Z-
1045 scores. Red indicates AML only observations, while gray indicates observations in all other cells.
1046 (b) same as (a) for ATOH8 vs. KNCK13 mixed Z-scores.
1047

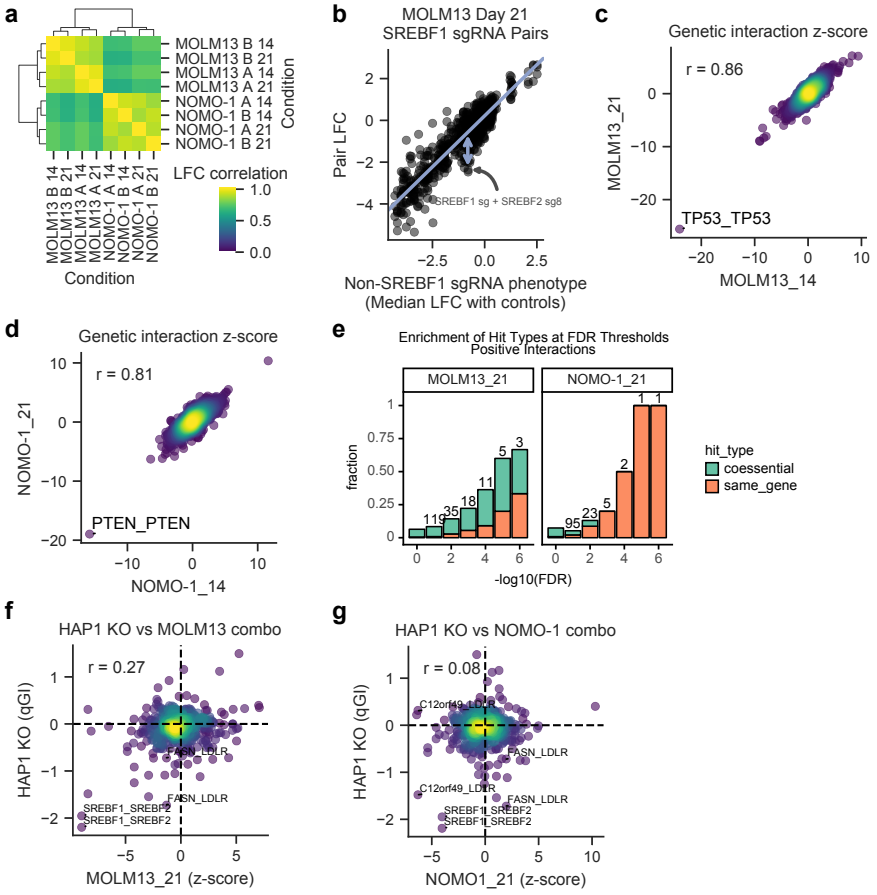

Figure S6

1048

1049

1050 **Figure S6. Combinatorial screen QC.** (a) Replicate correlations. (b) Example calculation of
1051 residuals. (c) Correlation between genetic interaction scores for MOLM13. (d) same as (c) for
1052 NOMO1. (e) Fraction of coessential pairs or pairs that target the same gene at different FDR
1053 cutoffs for interactions with positive z-scores. (f) Comparison with qGI scores from Aregger *et al.*
1054 for MOLM13. (g) Same as (f) for NOMO1.
1055

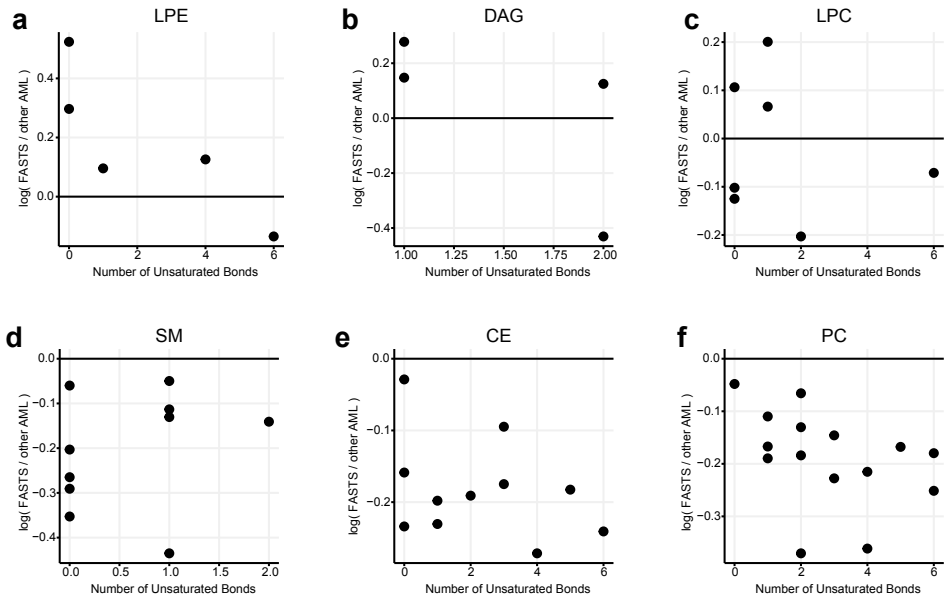

Figure S7

1056

1057

1058 **Figure S7. Additional metabolite comparisons.** (a) Lysophosphatidylethanolamine (LPE)
1059 species metabolite difference. The x axis represents the median difference of log10 normalized
1060 peak area of the metabolite in FASTS cells vs all other AML cells. The y axis represents the
1061 number of saturated bonds present. Each dot represents a unique metabolite. (b) same for
1062 diacylglycerol (DAG), (c) lysophosphatidylcholine (LPC), (d) sphingomyelin (SM), (e) cholesterol
1063 ester (CE), and (f) phosphatidylcholine (PC) species.
1064

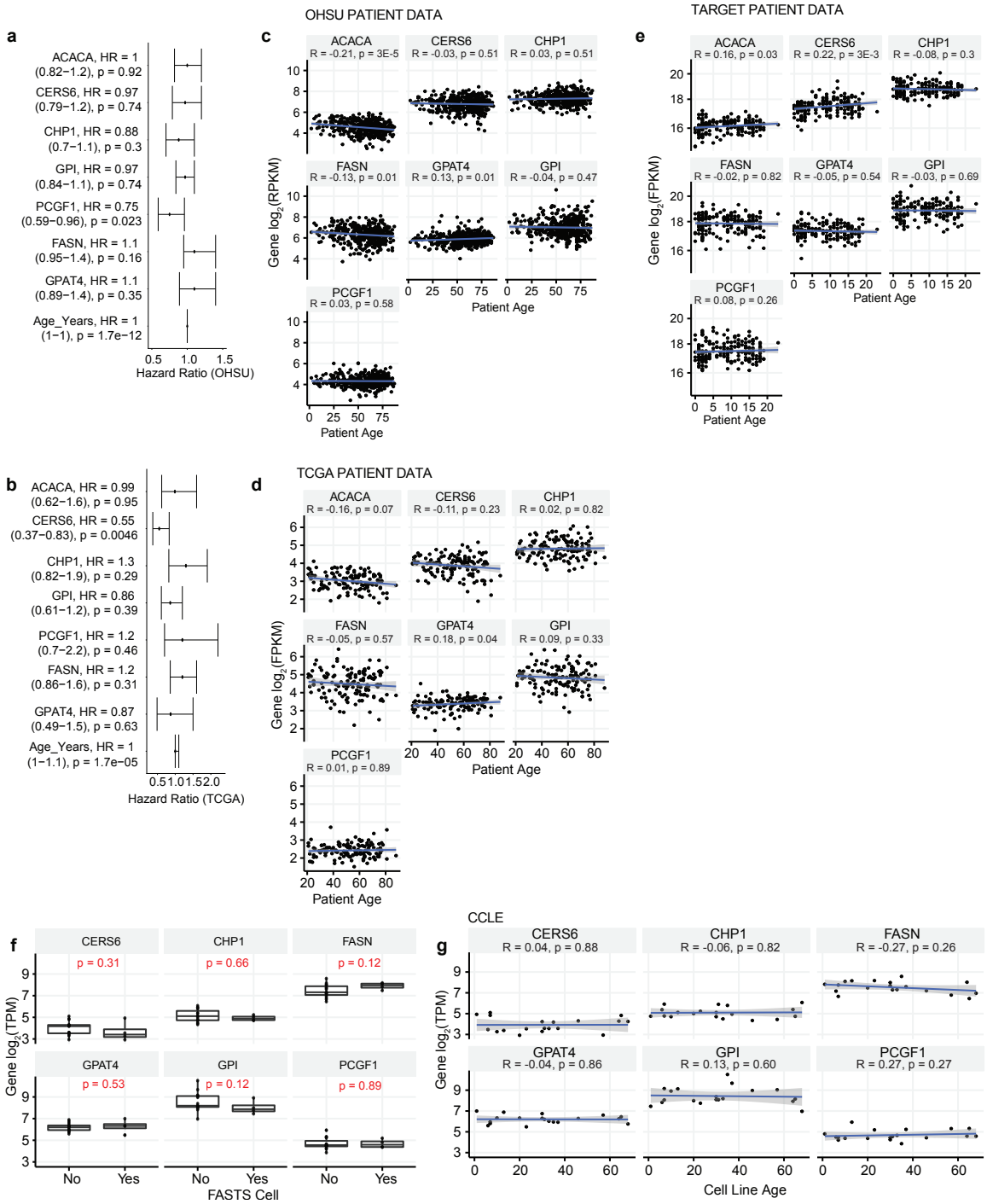
a
ACACA, HR = 1 (0.82−1.2), p = 0.92
CERS6, HR = 0.97 (0.79−1.2), p = 0.74
CHP1, HR = 0.88 (0.7−1.1), p = 0.3
GPI, HR = 0.97 (0.84−1.1), p = 0.74
PCGF1, HR = 0.75 (0.59−0.96), p = 0.023
FASN, HR = 1.1 (0.95−1.4), p = 0.16
GPAT4, HR = 1.1 (0.89−1.4), p = 0.35
Age_Years, HR = 1 (1−1), p = 1.7e−12
Hazard Ratio (OHSU)
b
ACACA, HR = 0.99 (0.62−1.6), p = 0.95
CERS6, HR = 0.55 (0.37−0.83), p = 0.0046
CHP1, HR = 1.3 (0.82−1.9), p = 0.29
GPI, HR = 0.86 (0.61−1.2), p = 0.39
PCGF1, HR = 1.2 (0.7−2.2), p = 0.46
FASN, HR = 1.2 (0.86−1.6), p = 0.31
GPAT4, HR = 0.87 (0.49−1.5), p = 0.63
Age_Years, HR = 1 (1−1.1), p = 1.7e−05
Hazard Ratio (TCGA)
c
OHSU PATIENT DATA
ACACA R = -0.21, p = 3E-5
CERS6 R = -0.03, p = 0.51
CHP1 R = 0.03, p = 0.51
FASN R = -0.13, p = 0.01
GPAT4 R = 0.13, p = 0.01
GPI R = -0.04, p = 0.47
PCGF1 R = 0.03, p = 0.58
Gene log2(RPKM)
Patient Age
d
TCGA PATIENT DATA
ACACA R = -0.16, p = 0.07
CERS6 R = -0.11, p = 0.23
CHP1 R = 0.02, p = 0.82
FASN R = -0.05, p = 0.57
GPAT4 R = 0.18, p = 0.04
GPI R = 0.09, p = 0.33
PCGF1 R = 0.01, p = 0.89
Gene log2(FPKM)
Patient Age
e
TARGET PATIENT DATA
ACACA R = 0.16, p = 0.03
CERS6 R = 0.22, p = 3E-3
CHP1 R = -0.08, p = 0.3
FASN R = -0.02, p = 0.82
GPAT4 R = -0.05, p = 0.54
GPI R = -0.03, p = 0.69
PCGF1 R = 0.08, p = 0.26
Gene log2(FPKM)
Patient Age
f
CERS6 p = 0.31
CHP1 p = 0.66
FASN p = 0.12
GPAT4 p = 0.53
GPI p = 0.12
PCGF1 p = 0.89
Gene log2(TPM)
No
Yes
FASTS Cell
g
CCLE
CERS6 R = 0.04, p = 0.88
CHP1 R = -0.06, p = 0.82
FASN R = -0.27, p = 0.26
GPAT4 R = -0.04, p = 0.86
GPI R = 0.13, p = 0.60
PCGF1 R = 0.27, p = 0.27
Gene log2(TPM)
Cell Line Age

1065

1066

1067 **Figure S8. Comparisons of FAS genes against age in AML patient data.** Hazard ratio
1068 calculations for FAS cluster genes in AML patient data coming from (a) OHSU - Tyner *et al.,* and
1069 (b) TCGA LAML. Spearman correlations of patient age against FAS gene expression in (c) OHSU,
1070 Tyner *et al.,* (d) TCGA LAML, and (e) GDC TARGET AML. (f) Boxplots of FAS gene expression
1071 in FASTS AML cell lines and non-FASTS AML cell lines from CCLE. (g) Spearman correlations
1072 of patient derived cell line age against FAS gene expression, coming from data in CCLE. ACACA
1073 is not included in (g) as it was not found in the CCLE expression data used in prior analysis.
1074

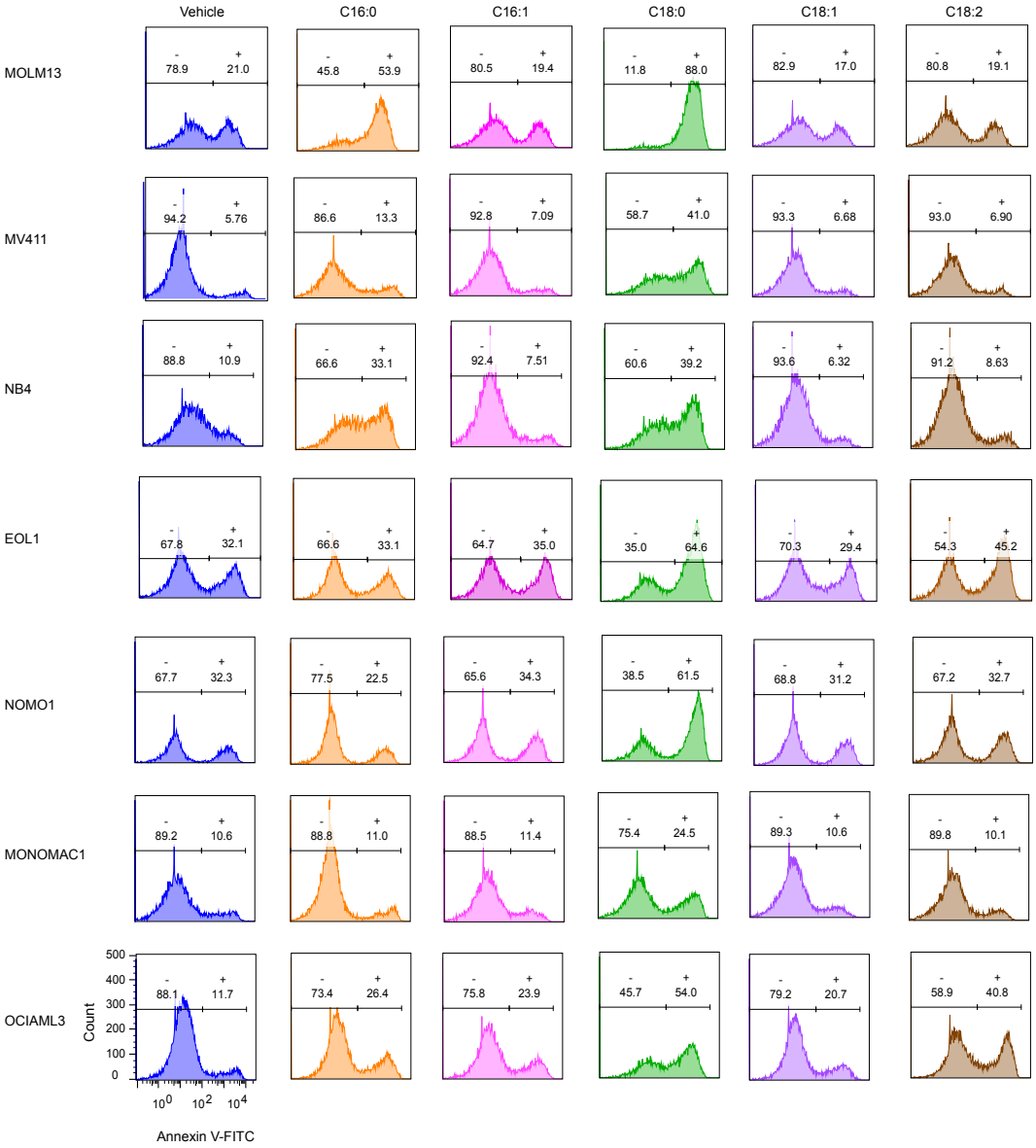

Figure S8

1075

1076

1077 **Figure S9. Sample flow cytometry plots.** A representative flow cytometry data used to create

1078 bar graphs shown in figure 5b-c.

1079

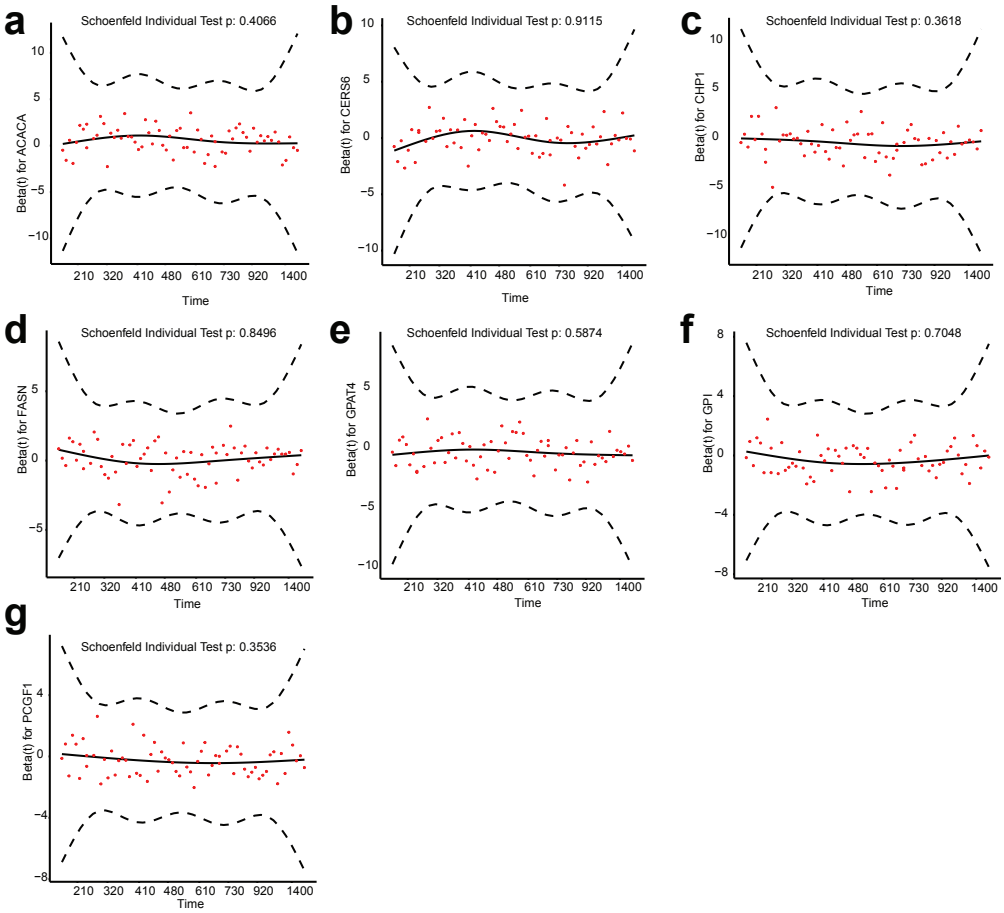
a
Schoenfeld Individual Test p: 0.4066
Beta(t) for ACACA
b
Schoenfeld Individual Test p: 0.9115
Beta(t) for CERS6
c
Schoenfeld Individual Test p: 0.3618
Beta(t) for CHP1
d
Schoenfeld Individual Test p: 0.8496
Beta(t) for FASN
e
Schoenfeld Individual Test p: 0.5874
Beta(t) for GPAT4
f
Schoenfeld Individual Test p: 0.7048
Beta(t) for GPI
g
Schoenfeld Individual Test p: 0.3536
Beta(t) for PCGF1
Time
210 320 410 480 610 730 920 1400

1082 **Figure S10. Testing the Cox Proportional Hazards Assumption.** Assessing the Cox
1083 proportional hazards assumption with Schoenfeld tests of all genes in Figure 6d; (a) ACACA, (b)
1084 CERS6, (c) CHP1, (d)FASN, (e) GPAT4, (f) GPI, (g) PCGF1.
1085
1086

1087 **References**

1088

1089 1. Jinek, M. *et al.* A Programmable Dual-RNA–Guided DNA Endonuclease in Adaptive Bacterial
1090 Immunity. *Science* **337**, 816–821 (2012).
1091 2. Mali, P. *et al.* RNA-Guided Human Genome Engineering via Cas9. *Science* **339**, 823–826
1092 (2013).
1093 3. Mali, P., Esvelt, K. M. & Church, G. M. Cas9 as a versatile tool for engineering biology.
1094 *Nature Methods* **10**, 957–963 (2013).
1095 4. Cong, L. *et al.* Multiplex genome engineering using CRISPR/Cas systems. *Science (New*
1096 *York, N.Y.)* **339**, 819–823 (2013).
1097 5. Shalem, O., Sanjana, N. E. & Zhang, F. High-throughput functional genomics using CRISPR-
1098 Cas9. *Nat. Rev. Genet.* **16**, 299–311 (2015).
1099 6. Wang, T., Wei, J. J., Sabatini, D. M. & Lander, E. S. Genetic screens in human cells using
1100 the CRISPR-Cas9 system. *Science* **343**, 80–84 (2014).
1101 7. Hart, T. *et al.* High-Resolution CRISPR Screens Reveal Fitness Genes and Genotype-
1102 Specific Cancer Liabilities. *Cell* **163**, 1515–1526 (2015).
1103 8. Wang, T. *et al.* Identification and characterization of essential genes in the human genome.
1104 *Science* **350**, 1096–1101 (2015).
1105 9. Aguirre, A. J. *et al.* Genomic Copy Number Dictates a Gene-Independent Cell Response to
1106 CRISPR/Cas9 Targeting. *Cancer Discovery* **6**, 914–929 (2016).
1107 10. Meyers, R. M. *et al.* Computational correction of copy number effect improves specificity
1108 of CRISPR-Cas9 essentiality screens in cancer cells. *Nat. Genet.* **49**, 1779–1784 (2017).
1109 11. Tsherniak, A. *et al.* Defining a Cancer Dependency Map. *Cell* **170**, 564-576.e16 (2017).
1110 12. Tzelepis, K. *et al.* A CRISPR Dropout Screen Identifies Genetic Vulnerabilities and
1111 Therapeutic Targets in Acute Myeloid Leukemia. *Cell Rep* **17**, 1193–1205 (2016).

1112 13. Behan, F. M. *et al.* Prioritization of cancer therapeutic targets using CRISPR-Cas9
1113 screens. *Nature* **568**, 511–516 (2019).
1114 14. Lagziel, S., Lee, W. D. & Shlomi, T. Inferring cancer dependencies on metabolic genes
1115 from large-scale genetic screens. *BMC biology* **17**, 37 (2019).
1116 15. Rossiter, N. J. *et al.* CRISPR screens in physiologic medium reveal conditionally
1117 essential genes in human cells. *Cell Metabolism* **33**, 1248-1263.e9 (2021).
1118 16. Zhao, D. *et al.* Combinatorial CRISPR-Cas9 Metabolic Screens Reveal Critical Redox
1119 Control Points Dependent on the KEAP1-NRF2 Regulatory Axis. *Molecular Cell* **69**, 699-
1120 708.e7 (2018).
1121 17. Aregger, M. *et al.* Systematic mapping of genetic interactions for de novo fatty acid
1122 synthesis identifies C12orf49 as a regulator of lipid metabolism. *Nature Metabolism* **2**, 499–
1123 513 (2020).
1124 18. Wang, T. *et al.* Gene Essentiality Profiling Reveals Gene Networks and Synthetic Lethal
1125 Interactions with Oncogenic Ras. *Cell* **168**, 890-903.e15 (2017).
1126 19. Boyle, E. A., Pritchard, J. K. & Greenleaf, W. J. High-resolution mapping of cancer cell
1127 networks using co-functional interactions. *Mol. Syst. Biol.* **14**, e8594 (2018).
1128 20. Rauscher, B. *et al.* Toward an integrated map of genetic interactions in cancer cells.
1129 *Molecular Systems Biology* **14**, e7656 (2018).
1130 21. Kim, E. *et al.* A network of human functional gene interactions from knockout fitness
1131 screens in cancer cells. *Life Science Alliance* **2**, (2019).
1132 22. Kegel, B. D. & Ryan, C. J. Paralog buffering contributes to the variable essentiality of
1133 genes in cancer cell lines. *PLOS Genetics* **15**, e1008466 (2019).
1134 23. Dede, M., McLaughlin, M., Kim, E. & Hart, T. Multiplex enCas12a screens detect
1135 functional buffering among paralogs otherwise masked in monogenic Cas9 knockout
1136 screens. *Genome Biology* **21**, 262 (2020).

1137 24. Beltrao, P., Cagney, G. & Krogan, N. J. Quantitative genetic interactions reveal
1138 biological modularity. *Cell* **141**, 739–745 (2010).
1139 25. Costanzo, M. *et al.* The genetic landscape of a cell. *Science* **327**, 425–431 (2010).
1140 26. Costanzo, M. *et al.* A global genetic interaction network maps a wiring diagram of
1141 cellular function. *Science* **353**, (2016).
1142 27. Martin, H. *et al.* Differential genetic interactions of yeast stress response MAPK
1143 pathways. *Molecular Systems Biology* **11**, 800 (2015).
1144 28. Wong, A. S. L. *et al.* Multiplexed barcoded CRISPR-Cas9 screening enabled by
1145 CombiGEM. *PNAS* **113**, 2544–2549 (2016).
1146 29. Shen, J. P. *et al.* Combinatorial CRISPR–Cas9 screens for de novo mapping of genetic
1147 interactions. *Nature Methods* **14**, 573–576 (2017).
1148 30. Han, K. *et al.* Synergistic drug combinations for cancer identified in a CRISPR screen for
1149 pairwise genetic interactions. *Nature Biotechnology* **35**, 463–474 (2017).
1150 31. Najm, F. J. *et al.* Orthologous CRISPR-Cas9 enzymes for combinatorial genetic screens.
1151 *Nature Biotechnology* **36**, 179–189 (2018).
1152 32. Du, D. *et al.* Genetic interaction mapping in mammalian cells using CRISPR
1153 interference. *Nat Methods* **14**, 577–580 (2017).
1154 33. Horlbeck, M. A. *et al.* Mapping the Genetic Landscape of Human Cells. *Cell* **174**, 953-
1155 967.e22 (2018).
1156 34. DeWeirdt, P. C. *et al.* Optimization of AsCas12a for combinatorial genetic screens in
1157 human cells. *Nature Biotechnology* 1–11 (2020) doi:10.1038/s41587-020-0600-6.
1158 35. Kleinstiver, B. P. *et al.* Engineered CRISPR-Cas12a variants with increased activities
1159 and improved targeting ranges for gene, epigenetic and base editing. *Nat. Biotechnol.* **37**,
1160 276–282 (2019).
1161 36. Bandyopadhyay, S. *et al.* Rewiring of genetic networks in response to DNA damage.
1162 *Science (New York, N.Y.)* **330**, 1385–1389 (2010).

1163 37. Ideker, T. & Krogan, N. J. Differential network biology. *Molecular Systems Biology* **8**, 565
1164 (2012).
1165 38. Colic, M. *et al.* Identifying chemogenetic interactions from CRISPR screens with drugZ.
1166 *Genome Med* **11**, 52 (2019).
1167 39. Menendez, J. A. & Lupu, R. Fatty acid synthase (FASN) as a therapeutic target in breast
1168 cancer. *Expert Opin. Ther. Targets* **21**, 1001–1016 (2017).
1169 40. Search of: FASN - List Results - ClinicalTrials.gov.
1170 https://clinicaltrials.gov/search?cond=FASN (2020).
1171 41. Hart, T. & Moffat, J. BAGEL: a computational framework for identifying essential genes
1172 from pooled library screens. *BMC Bioinformatics* **17**, 164 (2016).
1173 42. Kim, E. & Hart, T. Improved analysis of CRISPR fitness screens and reduced off-target
1174 effects with the BAGEL2 gene essentiality classifier. *Genome Medicine* **13**, 2 (2021).
1175 43. Allen, F. *et al.* JACKS: joint analysis of CRISPR/Cas9 knockout screens. *Genome Res.*
1176 **29**, 464–471 (2019).
1177 44. Daley, T. P. *et al.* CRISPhieRmix: a hierarchical mixture model for CRISPR pooled
1178 screens. *Genome Biol* **19**, 159 (2018).
1179 45. Bamford, S. *et al.* The COSMIC (Catalogue of Somatic Mutations in Cancer) database
1180 and website. *Br J Cancer* **91**, 355–358 (2004).
1181 46. Sondka, Z. *et al.* The COSMIC Cancer Gene Census: describing genetic dysfunction
1182 across all human cancers. *Nature Reviews Cancer* **18**, 696–705 (2018).
1183 47. Hart, T., Brown, K. R., Sircoulomb, F., Rottapel, R. & Moffat, J. Measuring error rates in
1184 genomic perturbation screens: gold standards for human functional genomics. *Molecular*
1185 *Systems Biology* **10**, 733 (2014).
1186 48. Dempster, J. M. *et al.* Extracting Biological Insights from the Project Achilles Genome-
1187 Scale CRISPR Screens in Cancer Cell Lines. *bioRxiv* 720243 (2019) doi:10.1101/720243.
1188 49. DepMap 20Q4 Public. (2020) doi:10.6084/m9.figshare.13237076.v4.

1189 50. James, M. F. *et al.* NF2/merlin is a novel negative regulator of mTOR complex 1, and
1190 activation of mTORC1 is associated with meningioma and schwannoma growth. *Mol. Cell.*
1191 *Biol.* **29**, 4250–4261 (2009).
1192 51. Huang, J., Dibble, C. C., Matsuzaki, M. & Manning, B. D. The TSC1-TSC2 complex is
1193 required for proper activation of mTOR complex 2. *Mol. Cell. Biol.* **28**, 4104–4115 (2008).
1194 52. Marchi, S. *et al.* Defective autophagy is a key feature of cerebral cavernous
1195 malformations. *EMBO Mol Med* **7**, 1403–1417 (2015).
1196 53. Zhu, Y. *et al.* Loss of endothelial programmed cell death 10 activates glioblastoma cells
1197 and promotes tumor growth. *Neuro-oncology* **18**, 538–548 (2016).
1198 54. Pópulo, H., Lopes, J. M. & Soares, P. The mTOR signalling pathway in human cancer.
1199 *Int J Mol Sci* **13**, 1886–1918 (2012).
1200 55. Massagué, J. G1 cell-cycle control and cancer. *Nature* **432**, 298–306 (2004).
1201 56. Evan, G. I. & Vousden, K. H. Proliferation, cell cycle and apoptosis in cancer. *Nature*
1202 **411**, 342–348 (2001).
1203 57. Donehower, L. A. *et al.* Integrated Analysis of TP53 Gene and Pathway Alterations in
1204 The Cancer Genome Atlas. *Cell Rep* **28**, 1370-1384.e5 (2019).
1205 58. Zhang, Y. *et al.* A Pan-Cancer Proteogenomic Atlas of PI3K/AKT/mTOR Pathway
1206 Alterations. *Cancer Cell* **31**, 820-832.e3 (2017).
1207 59. Pan, J. *et al.* Interrogation of Mammalian Protein Complex Structure, Function, and
1208 Membership Using Genome-Scale Fitness Screens. *Cell Syst* **6**, 555-568.e7 (2018).
1209 60. Bayraktar, E. C. *et al.* Metabolic coessentiality mapping identifies C12orf49 as a
1210 regulator of SREBP processing and cholesterol metabolism. *Nat Metab* **2**, 487–498 (2020).
1211 61. Hwang, S. *et al.* HumanNet v2: human gene networks for disease research. *Nucleic*
1212 *Acids Res* **47**, D573–D580 (2019).

1213 62. Khalid, A., Siddiqui, A. J., Huang, J.-H., Shamsi, T. & Musharraf, S. G. Alteration of
1214 Serum Free Fatty Acids are Indicators for Progression of Pre-leukaemia Diseases to
1215 Leukaemia. *Scientific Reports* **8**, 14883 (2018).
1216 63. Flavin, R., Peluso, S., Nguyen, P. L. & Loda, M. Fatty acid synthase as a potential
1217 therapeutic target in cancer. *Future Oncology* **6**, 551–562 (2010).
1218 64. Punekar, S. & Cho, D. C. Novel Therapeutics Affecting Metabolic Pathways. *American*
1219 *Society of Clinical Oncology Educational Book* e79–e87 (2019) doi:10.1200/EDBK_238499.
1220 65. Roguev, A. *et al.* Conservation and rewiring of functional modules revealed by an
1221 epistasis map in fission yeast. *Science* **322**, 405–410 (2008).
1222 66. Li, K.-C. Genome-wide coexpression dynamics: Theory and application. *Proc Natl Acad*
1223 *Sci U S A* **99**, 16875–16880 (2002).
1224 67. Piccolis, M. *et al.* Probing the Global Cellular Responses to Lipotoxicity Caused by
1225 Saturated Fatty Acids. *Molecular Cell* **74**, 32-44.e8 (2019).
1226 68. Zhu, X. G. *et al.* CHP1 Regulates Compartmentalized Glycerolipid Synthesis by
1227 Activating GPAT4. *Mol. Cell* **74**, 45-58.e7 (2019).
1228 69. Ghandi, M. *et al.* Next-generation characterization of the Cancer Cell Line Encyclopedia.
1229 *Nature* **569**, 503–508 (2019).
1230 70. Li, H. *et al.* The landscape of cancer cell line metabolism. *Nature Medicine* **25**, 850–860
1231 (2019).
1232 71. Meshinchi, S. & Arceci, R. TARGET: Acute Myeloid Leukemia (AML), dbGaP Study
1233 Accession: phs000465.v19.p8. https://www.ncbi.nlm.nih.gov/projects/gap/cgi-
1234 bin/study.cgi?study_id=phs000465.v19.p8 (2020).
1235 72. Genomic and Epigenomic Landscapes of Adult De Novo Acute Myeloid Leukemia. *New*
1236 *England Journal of Medicine* **368**, 2059–2074 (2013).
1237 73. Tyner, J. W. *et al.* Functional genomic landscape of acute myeloid leukaemia. *Nature*
1238 **562**, 526–531 (2018).

74. Grolemund, G. & Wickham, H. *R for Data Science*. (2020).

75. The R Development Core Team. *R: A Language and Environment for Statistical Computing*. (2016).

76. Python Software Foundation. *Python Language Reference, version 3.8.2*. (2020).

77. Virtanen, P. *et al.* SciPy 1.0: fundamental algorithms for scientific computing in Python. *Nature Methods* **17**, 261–272 (2020).

78. Harris, C. R. *et al.* Array programming with NumPy. *Nature* **585**, 357–362 (2020).

79. Hunter, J. D. Matplotlib: A 2D Graphics Environment. *Computing in Science Engineering* **9**, 90–95 (2007).

80. McKinney, W. Data Structures for Statistical Computing in Python. *Proceedings of the 9th Python in Science Conference* 56–61 (2010) doi:10.25080/Majora-92bf1922-00a.

81. Wickham, H. *et al.* Welcome to the Tidyverse. *Journal of Open Source Software* **4**, 1686 (2019).

82. Dowle, M. *et al. data.table: Extension of 'data.frame'*. (2020).

83. Xie, Y. *et al. knitr: A General-Purpose Package for Dynamic Report Generation in R*. (2020).

84. Xie, Y. knitr: A Comprehensive Tool for Reproducible Research in R. *Implementing Reproducible Research* 3–31 https://www.taylorfrancis.com/ (2018) doi:10.1201/9781315373461-1.

85. Xie, Y. Dynamic Documents with R and knitr. *Routledge & CRC Press* https://www.routledge.com/Dynamic-Documents-with-R-and-knitr-2nd-Edition/Xie/p/book/9781498716963 (2015).

86. Benaglia, T., Chauveau, D., Hunter, D. & Young, D. mixtools: An R Package for Analyzing Finite Mixture Models. *Journal of Statistical Software* **32**, (2009).

87. Simpson, G. L., R Core Team, Bates, D. M. & Oksanen, J. *permute: Functions for Generating Restricted Permutations of Data*. (2019).

1265 88. Keilwagen, J., Grosse, I. & Grau, J. Area under Precision-Recall Curves for Weighted
1266 and Unweighted Data. *PLOS ONE* **9**, e92209 (2014).
1267 89. Grau, J., Grosse, I. & Keilwagen, J. PRROC: computing and visualizing precision-recall
1268 and receiver operating characteristic curves in R. *Bioinformatics* **31**, 2595–2597 (2015).
1269 90. Durinck, S., Spellman, P. T., Birney, E. & Huber, W. Mapping identifiers for the
1270 integration of genomic datasets with the R/Bioconductor package biomaRt. *Nat Protoc* **4**,
1271 1184–1191 (2009).
1272 91. Durinck, S. *et al.* BioMart and Bioconductor: a powerful link between biological
1273 databases and microarray data analysis. *Bioinformatics* **21**, 3439–3440 (2005).
1274 92. Carlson, M. org.Hs.eg.db. *Bioconductor* http://bioconductor.org/packages/org.Hs.eg.db/
1275 (2018).
1276 93. Wilke, C. Streamlined Plot Theme and Plot Annotations for 'ggplot2'.
1277 https://wilkelab.org/cowplot/ (2019).
1278 94. Clarke, E. & Sherrill-Mix, S. *ggbeeswarm: Categorical Scatter (Violin Point) Plots*.
1279 (2017).
1280 95. Gentleman, R. *annotate: Annotation for microarrays*. (Bioconductor version: Release
1281 (3.11), 2020). doi:10.18129/B9.bioc.annotate.
1282 96. Neuwirth, E. *RColorBrewer: ColorBrewer Palettes*. (2014).
1283 97. Gu, Z., Eils, R. & Schlesner, M. Complex heatmaps reveal patterns and correlations in
1284 multidimensional genomic data. *Bioinformatics* **32**, 2847–2849 (2016).
1285 98. Warnes, G. R. *et al. gplots: Various R Programming Tools for Plotting Data*. (2020).
1286 99. Kassambara, A. ggplot2 Based Publication Ready Plots.
1287 https://rpkgs.datanovia.com/ggpubr/ (2020).
1288 100. Gu, Z., Gu, L., Eils, R., Schlesner, M. & Brors, B. circlize Implements and enhances
1289 circular visualization in R. *Bioinformatics* **30**, 2811–2812 (2014).
1290 101. Arnold, J. B. *et al. ggthemes: Extra Themes, Scales and Geoms for 'ggplot2'*. (2019).

102. Attali, D. & Baker, C. *ggExtra: Add Marginal Histograms to 'ggplot2', and More 'ggplot2' Enhancements*. (2019).

103. Pedersen, T. L. *patchwork: The Composer of Plots*. (2020).

104. Wickham, H. *ggplot2: Elegant Graphics for Data Analysis*. (Springer, 2016).

105. Therneau, T. M. & Grambsch, P. M. *Modeling Survival Data: Extending the Cox Model*. (Springer-Verlag, 2000). doi:10.1007/978-1-4757-3294-8.

106. Therneau, T. M., until 2009), T. L. (original S.->R port and R. maintainer, Elizabeth, A. & Cynthia, C. *survival: Survival Analysis*. (2020).

107. Kassambara, A., Kosinski, M., Biecek, P. & Fabian, S. *survminer: Drawing Survival Curves using 'ggplot2'*. (2020).

108. Python Software Foundation. *Python Language Reference, version 3.8.5*. (2020).

109. Waskom, M. L. seaborn: statistical data visualization. *Journal of Open Source Software* **6**, 3021 (2021).

110. Plotly Technologies Inc. Collaborative data science. (2015).

111. Davidson-Pilon, C. *et al. CamDavidsonPilon/lifelines: 0.26.0*. (Zenodo, 2021). doi:10.5281/zenodo.4816284.

112. Python Software Foundation. *Python Language Reference, version 3.8.3*. (2020).

113. Pedersen, T. L. *tidygraph: A Tidy API for Graph Manipulation*. (2020).

114. Pedersen, T. L. & RStudio. *ggraph: An Implementation of Grammar of Graphics for Graphs and Networks*. (2020).

115. Seabold, S. & Perktold, J. Statsmodels: Econometric and Statistical Modeling with Python. 5 (2010).

116. Hassan Kibirige *et al. has2k1/plotnine: v0.7.1*. (Zenodo, 2020). doi:10.5281/zenodo.3973626.

117. DeWeirdt, P. C. *gnt: Python packcage for caidentifying Genetic iNTeractions from combinatorial screening data.* (2020).

1317 118. DeWeirdt, P. C. *gpplot: Plotting functions for the Genetic Perturbation Platform's R&D*
1318 *group at the Broad institute.* (2020).
1319 119. Pujar, S. *et al.* Consensus coding sequence (CCDS) database: a standardized set of
1320 human and mouse protein-coding regions supported by expert curation. *Nucleic Acids Res.*
1321 **46**, D221–D228 (2018).
1322 120. Iorio, F. *et al.* Unsupervised correction of gene-independent cell responses to CRISPR-
1323 Cas9 targeting. *BMC Genomics* **19**, 604 (2018).
1324 121. Frankish, A. *et al.* GENCODE reference annotation for the human and mouse genomes.
1325 *Nucleic Acids Res* **47**, D766–D773 (2019).
1326 122. Zerbino, D. R. *et al.* Ensembl 2018. *Nucleic Acids Res* **46**, D754–D761 (2018).
1327 123. Hart, T. *et al.* Evaluation and Design of Genome-Wide CRISPR/SpCas9 Knockout
1328 Screens. *G3 (Bethesda)* **7**, 2719–2727 (2017).
1329 124. Shannon, P. *et al.* Cytoscape: A Software Environment for Integrated Models of
1330 Biomolecular Interaction Networks. *Genome Res* **13**, 2498–2504 (2003).
1331 125. Luo, Y., Rana, P. & Will, Y. Palmitate increases the susceptibility of cells to drug-induced
1332 toxicity: an in vitro method to identify drugs with potential contraindications in patients with
1333 metabolic disease. *Toxicol. Sci.* **129**, 346–362 (2012).
1334 126. Alsabeeh, N., Chausse, B., Kakimoto, P. A., Kowaltowski, A. J. & Shirihai, O. Cell culture
1335 models of fatty acid overload: Problems and solutions. *Biochim Biophys Acta Mol Cell Biol*
1336 *Lipids* **1863**, 143–151 (2018).
1337 127. Gao, J. *et al.* Integrative analysis of complex cancer genomics and clinical profiles using
1338 the cBioPortal. *Sci Signal* **6**, pl1 (2013).
1339 128. Cerami, E. *et al.* The cBio Cancer Genomics Portal: An Open Platform for Exploring
1340 Multidimensional Cancer Genomics Data. *Cancer Discov* **2**, 401–404 (2012).
1341 129. German Collection of Microorganisms and Cell Cultures GmbH: Welcome to the Leibniz
1342 Institute DSMZ. https://www.dsmz.de/ (2020).

130. Goldman, M. J. *et al.* Visualizing and interpreting cancer genomics data via the Xena platform. *Nature Biotechnology* **38**, 675–678 (2020).

131. Bairoch, A. The Cellosaurus, a Cell-Line Knowledge Resource. *J Biomol Tech* **29**, 25–38 (2018).